Composites Science and Technology 254 (2024) 110634

Contents lists available at ScienceDirect

Composites Science and Technology

journal homepage: www.elsevier.com/locate/compscitech

A three-dimensional viscoelastic–viscoplastic and viscodamage constitutive model for unidirectional fibre-reinforced polymer laminates

I.R. Cózar [a,*], P. Maimí [a], E.V. González [a], P.P. Camanho [b,c], F. Otero [d,e]

[a] AMADE, Polytechnic School, University of Girona, Campus Montilivi s/n, 17071 Girona, Spain
[b] DEMec, Faculdade de Engenharia, Universidade do Porto, 4200-465 Porto, Portugal
[c] INEGI, Instituto de Ciência e Inovação em Engenharia Mecânica e Industrial, 4200-465 Porto, Portugal
[d] CIMNE, Universitat de Politècnica de Catalunya, 08034 Barcelona, Spain
[e] Department of Nautical Science and Engineering, Universitat Politècnica de Catalunya. Pla de Palau 18, 08003 Barcelona, Spain

ARTICLE INFO

Keywords:
C. Computational mechanics
C. Damage mechanics
C. Finite element analysis (FEA)
C. Material modelling
C. Stress relaxation

ABSTRACT

A novel 3D viscoelastic–viscoplastic and viscodamage constitutive model is proposed to predict the viscous effects due to dynamic loading conditions of unidirectional carbon fibre-reinforced polymer laminates at the meso-scale level. The present model is developed under continuum damage mechanics and the thermodynamics of irreversible processes framework. The viscoelastic response is modelled using the generalised Maxwell model, while an overstress model is employed to address the viscoplastic strain. The onset of the viscodamage mechanisms is based on experimental expressions, and their propagation is defined as a function of the corresponding fracture toughness. The mechanical response of the present constitutive model under pure longitudinal shear loading conditions at different strain rates is presented. The higher the strain rate is, the stiffer the responses in the viscoelastic and viscoplastic regions are. Additionally, the onset of viscodamage increases with higher strain rates. Off-axis compressive experimental data at two different strain rates are employed to demonstrate the capabilities of the present model with good predictions being obtained.

1. Introduction

The use of carbon fibre-reinforced polymer (CFRP) laminates to manufacture of aircraft components has increased in recent years due to its high stiffness and strength, low density and high fatigue resistance [1–3]. CFRPs are widely employed in major-load bearing structures, replacing older aircraft structures which were mainly made of aluminium. CFRP laminates are also employed in the automotive sector to reduce pollutant emissions by decreasing vehicle weight, thereby improving energy efficiency in both internal combustion engine vehicles [3–5] and electric vehicles [6–9]. In general, composite material components in these sectors are subjected to dynamic loading, such as impacts [10–13].

Numerous experimental investigations have been carried out to understand the dynamic effects on CFRPs. For instance, Hsiao et al. [14] performed off-axis compressive tests under quasi-static and dynamic loading conditions using a CFRP laminate. The authors observed a strain rate dependency on the stress–strain behaviour, along with an increase in off-axis compressive strength and modulus of elasticity at high strain rates. In addition, as the loading rate is increased, the plastic hardening response in compression also increases. However, the ultimate compressive strain decreases for off-axis angles less or equal to 45°. No significant strain rate dependency on the ultimate strain was found in off-axis compressive tests for off-axis angles greater than 60° [15–17]. Vinson and Woldesenbet [18] observed that the strain rate sensitivity of the failure compressive strength decreases as the off-axis angle increases because the failure mode changes. The off-axis tensile strength and the elastic modulus also increases with increasing loading rates [17,19]. Likewise, the longitudinal shear modulus, yielding stress and strength also increase in the in-plane shear test at higher strain rates [20,21].

Ploeckl et al. [22] carried out compressive tests using a quasi-isotropic laminate with a CFRP under different loading rates. Although the authors reported no significant strain rate effects on the elastic modulus, the compressive strength and the ultimate strain do increase with higher loading rates. Similar behaviour is observed for unidirectional CFRP laminates under longitudinal compressive loading conditions [22–26]. In contrast, no significant strain rate dependency on the stress–strain response under longitudinal tensile conditions has been found for unidirectional CFRP [27,28]. Jacob et al. [29] reported no significant difference from quasi-static to dynamic loading conditions

* Corresponding author.
E-mail address: ivan.ruiz@udg.edu (I.R. Cózar).

https://doi.org/10.1016/j.compscitech.2024.110634
Received 5 February 2024; Received in revised form 26 April 2024; Accepted 30 April 2024
Available online 29 May 2024

for the longitudinal tensile and compressive strengths. Cheng et al. [30] carried out quasi-static and dynamic compact tensile tests in a cross-ply CFRP laminate, finding no clear trend of the longitudinal tensile fracture toughness as a function of the strain rate. However, other authors have reported the strain rate having a significant effect on the longitudinal tensile fracture toughness (this material property decreased with increasing strain rate) [31,32]. Depending on the data reduction methods and testing techniques employed, fracture toughness increases or decreases as a function of the loading rate conditions.

Kuhn et al. [33] performed double-edge notched compressive tests using different loading rates and specimen sizes on cross-ply CFRP laminates. The authors reported a strong dependency of the strain rate on the longitudinal compressive fracture toughness, with its value being greater at higher strain rates. In addition, the cross-ply CFRP laminates exhibited a strain rate effect on the elastic stiffness, where its value increases with strain rate increases, but the ultimate strain decreases when increasing the loading rate [34,35]. Perry and Walley [26] observed an increase in the cross-ply elastic modulus in compression with increasing loading rates, but no significant strain rate effect was found in tension [34].

Consequently, the dynamic effects must be considered in constitutive models for CFRPs to predict the inelastic deformation and fracture under dynamic loading conditions. Koerber et al. [19] developed a 3D constitutive model for CFRPs which considers plastic deformations with a failure criterion for damage onset (no damage propagation was considered). A non-associated plastic flow rule was defined using the overstress function proposed by Perzyna [36]. The strain rate effects in the elastic and strength properties were considered by introducing experimentally-obtained scaling functions. Kang et al. [37] presented a 3D constitutive model to predict the inelastic deformation in a dynamic tensile biaxial test using a CFRP laminate. An isotropic yield function was defined by combining the Tsai–Hill equivalent stress criterion and the Voce-type strain-hardening law. The strain rate dependency was introduced by scaling the isotropic term of the yield criterion as a function of the strain rate. In numerous studies of constitutive models for CRPF materials, scaling functions are applied to the material properties to account for the strain rate dependency on the elastic region [38–41], as well as on the plastic and damage regions [42–45].

Chang et al. [46] developed a viscoelastic constitutive model based on the generalised Maxwell model. The non-linear stress–strain relationships of CFRPs in the elastic region resulting from different loading rate and temperature conditions were predicted. Gerbaud et al. [47] proposed a 3D viscoelastic–viscoplastic model for CFRPs, and the model was extended to finite strain theory [48]. The generalised Maxwell model was employed to consider the viscous effects in the elastic region due to strain rates. The loading strain rate dependency on the plastic region was introduced by a non-associative plastic flow rule using the overstress model [36]. Hegde and Mulay [49] developed a 1D viscoelastic damage model for viscoelastic matrix materials. Again, the generalised Maxwell model was used and coupled to a damage model. A single damage variables were employed to degrade: (i) the quasi-static stiffness and (ii) the stiffness of the Maxwell element.

From observations in the literature, no 3D constitutive model addressees modelling CFRPs by considering the viscoelastic–viscoplastic behaviour to account for viscodamage evolution and fracture toughness. Table 1 summarises the features of the published constitutive models that account for strain rate dependency. Currently, there are only two constitutive models that account for the viscoelastic, viscoplastic and viscodamage effects of CFRPs [19,38], but the scale functions being used in the viscoelastic region can induce thermodynamic inconsistencies as the strain rates change. Furthermore, Koerber et al. [19] only modelled the initiation, not the propagation of the failure.

In the present work, a 3D viscoelastic–viscoplastic and viscodamage model is proposed to predict the constitutive behaviour of CFRPs under dynamic loading conditions. The proposed constitutive model is based on the generalised Maxwell viscoelastic model and the overstress viscoplastic model. The onset of the damage is developed using experimental scale functions. Failure propagation is defined by softening laws that take into account the energy dissipated by the corresponding viscodamage process. The constitutive model is described in Section 2. In Section 3, a simple longitudinal shear virtual test at different loading rates and a relaxation test are carried out to verify the stress–strain response of the proposed constitutive model at the Gauss-point level. In addition, a numerical–experimental comparison of off-axis compressive tests at different loading rates is performed to demonstrate the predictive capabilities of the model. Finally, the main conclusions of the present work are summarised in Section 4.

Table 1
Modelling strategies used in the literature to address the dynamic effects in CFRP laminates, where V refers to a strain-rate dependent (viscous) procedure and I refers to a strain-rate independent approach.

Authors	Elasticity	Plasticity	Damage	
			Initiation	Propagation
Koerber et al. [19]	V[a]	V[b]	V[a]	–
Kang et al. [37]	I	V[a]	–	
Eskandari et al. [38]	V[a]	V[b]	V[a]	
Tan and Liu [39]	V[a]	V[a]	–	
Shi et al. [40]	V[a]	–	V[a]	
Jin et al. [41]	V[a]	–	V[a]	
Raimondo et al. [42]	I	V[a]	V[a]	
Daniel [43]	I	–	V[a]	
Daniel [44]	I	V[a]	V[a]	
Ma et al. [45]	I	–	V[a]	
Chang et al. [46]	V[c]	–	–	
Gerbaud et al. [47]	V[c]	V[b]	–	
Lopes et al. [48]	V[c]	V[b]	–	
Hegde and Mulay [49]	V[c]	–	I	

[a] Using scale functions.
[b] Using the Overstress model [36].
[c] Using the generalised Maxwell model.

2. Constitutive model

The 3D elastoplastic damage model developed by Cózar et al. [50,51] is extended here to include the viscous effects due to dynamic loading conditions. Different hypothesis have been considered to develop the constitutive model from the experimental observations available in the literature: (i) the longitudinal direction (fibre dominated direction) is strain rate-independent, except its strength; (ii) a viscoelastic and viscoplastic behaviour is considered in the directions governed by the matrix; (iii) damage related properties, strengths and fracture toughness can be defined as strain rate-dependent; and (iv) bilinear softening laws are considered in the longitudinal compressive and tensile directions and linear for the rest of the directions (as in the original model [50,51]).

The additive decomposition of the infinitesimal strain tensor is considered

$$\boldsymbol{\varepsilon} = \boldsymbol{\varepsilon}^{ve} + \boldsymbol{\varepsilon}^{vp}, \tag{1}$$

where $\boldsymbol{\varepsilon}^{ve}$ is the viscoelastic strain tensor that contains the cracking strains and $\boldsymbol{\varepsilon}^{vp}$ is the viscoplastic strain tensor. The model assumes purely elastic response before the onset of damage in the longitudinal direction. No significant dependence of the strain rates in neither the longitudinal Young's modulus, or in the inelastic deformation was observed in the literature for CFRP laminates for both tensile and compressive longitudinal loading directions [22–28] (see Fig. 1a). However, in the transverse directions, strong strain rate dependency on the elastic modulus and during the hardening process in CFRPs was observed [14,15,17,17,19–21]. Then, a viscoelastic response followed to a viscoplastic behaviour in the directions governed to the matrix is considered. After that, the onset of damage can be reached in any direction, and develops without increasing the viscoplastic strains at the Gauss-point level, see Fig. 1.

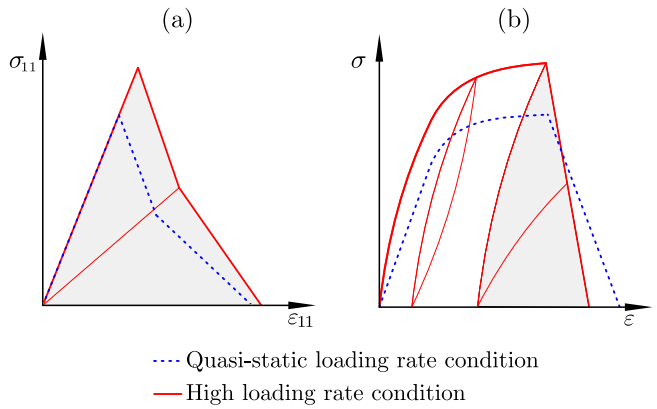

Fig. 1. Schematic representation of uniaxial stress vs. strain curve response at the Gauss-point level: (a) in the longitudinal direction, and (b) in the directions governed by the matrix.

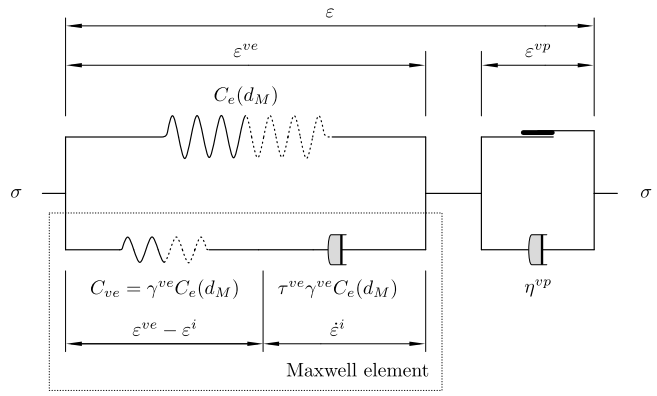

Fig. 2. Schematic representation of the 1D rheological scheme of the proposed constitutive model.

2.1. Modelling viscoelasticity

The viscoelastic effects of CFRPs under different loading rate conditions is modelled using the generalised Maxwell model. The 1D rheological scheme of the viscoelastic part can be divided into two main elements connected in parallel (see Fig. 2): (i) the Hookean element and (ii) the Maxwell element, which consists of a Hookean element and a Newtonian dashpot connected in series. The Hookean element (top left branch in Fig. 2) provides the quasi-static stiffness that remains after the dynamic effects have relaxed as the dashpot releases the Maxwell element (bottom left branch in Fig. 2). The original model [50,51] is proposed to be extended with a single Maxwell element to account for dynamic effects without significantly increasing the complexity of the calibration of the input model parameters in the viscoelastic region. To adjust the viscoelastic parameters, two tests can be used: a creep test and a uniaxial transverse test, as explained at the end of this section.

The Helmholtz free-energy density function proposed in Voigt notation reads

$$\Psi := \frac{1}{2}(\boldsymbol{\varepsilon} - \boldsymbol{\varepsilon}^{vp})^T \mathbb{C}_e (\boldsymbol{\varepsilon} - \boldsymbol{\varepsilon}^{vp}) + \frac{1}{2}(\boldsymbol{\varepsilon} - \boldsymbol{\varepsilon}^{vp} - \boldsymbol{\varepsilon}^{i})^T \mathbb{C}_{ve} (\boldsymbol{\varepsilon} - \boldsymbol{\varepsilon}^{vp} - \boldsymbol{\varepsilon}^{i}), \tag{2}$$

where $\boldsymbol{\varepsilon}^{i}$ is the inelastic strain tensor due to viscoelastic effects, and $\mathbb{C}_e$ and $\mathbb{C}_{ve}$ are the quasi-static and Maxwell elasticity tensors, respectively, see Fig. 2. The viscoelastic effects in CFRP laminates are only observed in the directions governed by the matrix (in the transverse isotropic plane with respect to the longitudinal direction). Therefore, $\mathbb{C}_{ve}$ is defined proportional to $\mathbb{C}_e$ in the direction governed by the matrix as

$$\mathbb{C}_{ve} := \boldsymbol{\Gamma} \mathbb{C}_e \boldsymbol{\Gamma}, \tag{3}$$

with

$$\boldsymbol{\Gamma} = \bar{\gamma}^{ve} \mathbb{I}^{ve}, \tag{4}$$

where $\bar{\gamma}^{ve}$ is a viscoelastic parameter and $\mathbb{I}^{ve}$ is the identity matrix with the first component equal to zero (longitudinal direction). Based on this hypothesis, a single relaxation time of the Newtonian dashpot of the Maxwell element (τ^{ve}) is defined for the directions governed by the matrix [47]. Therefore, the stress equilibrium in the Maxwell element (bottom left branch in Fig. 2) reads

$$\boldsymbol{\Gamma} \mathbb{C}_e \boldsymbol{\Gamma} (\boldsymbol{\varepsilon} - \boldsymbol{\varepsilon}^{vp} - \boldsymbol{\varepsilon}^{i}) = \boldsymbol{\Gamma} \mathbb{C}_e \boldsymbol{\Gamma} \mathbb{T}^{ve} \dot{\boldsymbol{\varepsilon}}^{i}, \tag{5}$$

where $\mathbb{T}^{ve} = \tau^{ve}\mathbf{I}$ ($\mathbf{I}$ is the identity matrix). These two assumptions allow the implementation of the constitutive model to be simplified. The use of a single τ^{ve} allows the differential equation for the stress (or strain) on the Maxwell element in 1D to be solved and extending it directly to 3D [47]. Furthermore, the viscoelastic strain rate dependence of CFRP plies can be characterised by two viscoelastic parameters.

The quasi-static elasticity tensor is defined using the compliance tensor ($\mathbb{H} = \mathbb{C}_e^{-1}$) proposed by Quintanas-Corominas et al. [52],

$$\mathbb{H} = \begin{bmatrix} \mathbb{H}_{11} & \mathbb{H}_{12} & \mathbb{H}_{12} & 0 & 0 & 0 \\ \mathbb{H}_{12} & \mathbb{H}_{22} & \mathbb{H}_{23} & 0 & 0 & 0 \\ \mathbb{H}_{12} & \mathbb{H}_{23} & \mathbb{H}_{22} & 0 & 0 & 0 \\ 0 & 0 & 0 & \mathbb{H}_{44} & 0 & 0 \\ 0 & 0 & 0 & 0 & \mathbb{H}_{55} & 0 \\ 0 & 0 & 0 & 0 & 0 & \mathbb{H}_{55} \end{bmatrix} \tag{6}$$

with:

$$\begin{aligned} \mathbb{H}_{11} &= \frac{1}{(1-d_\ell)E_{11}} \\ \mathbb{H}_{12} &= -\frac{\nu_{12}}{E_{11}} \\ \mathbb{H}_{22} &= \frac{1}{4(1-d_t)E_t} + \frac{1}{4(1-d_{st})G_t} \\ \mathbb{H}_{23} &= \frac{1}{4(1-d_t)E_t} - \frac{1}{4(1-d_{st})G_t} \\ \mathbb{H}_{44} &= \frac{1}{(1-d_{st})G_t} \\ \mathbb{H}_{55} &= \frac{1}{(1-d_{s\ell})G_{12}}, \end{aligned} \tag{7}$$

where E_{11} is the longitudinal elastic modulus, ν_{12} is the longitudinal Poisson's ratio, and G_{12} is the longitudinal shear elastic modulus. E_t is the elastic modulus associated to a change of area in the transverse isotropic plane, and G_t is the elastic modulus associated to a change of shape in the transverse isotropic plane. They are defined as

$$E_t := \frac{E_{22}}{2(1-\nu_{23})}, \tag{8}$$

and

$$G_t := \frac{E_{22}}{2(1+\nu_{23})}, \tag{9}$$

where E_{22} is the transverse elastic modulus and ν_{23} is the transverse Poisson's ratio.

The four viscodamage variables d_M ($M = \ell, t, s\ell, st$) defined in Eq. (7) describe the following failure mechanisms: d_ℓ associated to the longitudinal failure, d_t describes the mode-I matrix cracking, d_{st} associated to the mode-II matrix cracking, and $d_{s\ell}$ combines the longitudinal tensile and matrix failure mechanisms. Subscript ℓ refers to longitudinal, t to transverse, and s to shear.

The mechanical dissipated energy is defined from the Clausius–Duhem inequality to ensure the thermodynamically consistency of the model and the irreversibility of the dissipated processes [53].

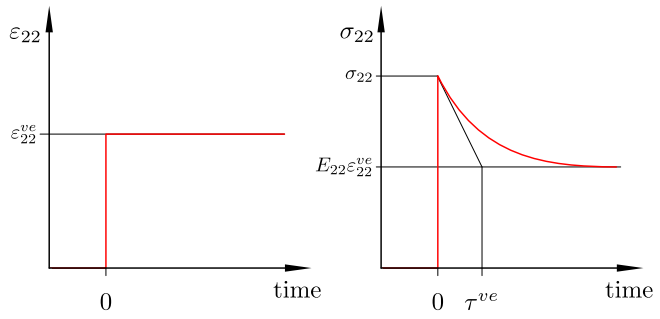

Fig. 3. Schematic representation of a transverse tensile test to measure the relaxation time of the Newtonian dashpot of the Maxwell element (τ^{ve}).

Considering an isothermal state, an energy dissipation carried out in an adiabatic manner, and a constant density, the Clausius–Duhem inequality reads

$$\Xi = \boldsymbol{\sigma}^T \dot{\boldsymbol{\varepsilon}} - \dot{\Psi} \geq 0, \tag{10}$$

where Ξ is the mechanical energy dissipated per unit volume. Applying the corresponding chain rules in Eq. (2), the inequality of Eq. (10) yields

$$\left(\boldsymbol{\sigma}^T - \frac{\partial \Psi}{\partial \boldsymbol{\varepsilon}}\right)\dot{\boldsymbol{\varepsilon}} - \frac{\partial \Psi}{\partial \boldsymbol{\varepsilon}^i}\dot{\boldsymbol{\varepsilon}}^i - \frac{\partial \Psi}{\partial \boldsymbol{\varepsilon}^{vp}}\dot{\boldsymbol{\varepsilon}}^{vp} - \sum_M \frac{\partial \Psi}{\partial d_M}\dot{d}_M \geq 0. \tag{11}$$

The expression in parenthesis of the first term in Eq. (11) must be equal to zero to guarantee this inequality since the strains can freely vary, yielding the constitutive equation:

$$\boldsymbol{\sigma} := \frac{\partial \Psi}{\partial \boldsymbol{\varepsilon}}, \tag{12}$$

where $\boldsymbol{\sigma}$ is the stress tensor that can be rewritten from the generalised Maxwell model as

$$\boldsymbol{\sigma} = \mathbb{C}_e(\boldsymbol{\varepsilon} - \boldsymbol{\varepsilon}^{vp}) + \boldsymbol{\Gamma}\mathbb{C}_e\boldsymbol{\Gamma}(\boldsymbol{\varepsilon} - \boldsymbol{\varepsilon}^{vp} - \boldsymbol{\varepsilon}^i). \tag{13}$$

The demonstration of the non-negativity of the rest of the terms of Eq. (11) is presented in Appendix.

The relaxation time of the Newtonian dashpot of the Maxwell element (τ^{ve}) can be measured through a relaxation test from the tangent line where the material starts to relax ($\boldsymbol{\sigma}_{22}$) and the stress relaxed ($E_{22}\boldsymbol{\varepsilon}_{22}^{ve}$) [54], see Fig. 3. Additionally, for a given τ^{ve}, the viscoelastic parameter ($\bar{\gamma}^{ve}$) can be fitted from an experimental transverse tensile test at constant loading rate. The transverse stress Cartesian component applying uniaxial transverse stress state conditions in Eq. (13) at constant strain rate yields

$$\boldsymbol{\sigma}_{22} = E_{22}\left(1 + \gamma^{ve}\tau^{ve}\dot{\boldsymbol{\varepsilon}}_{22}^{ve}\left(1 - \exp\left(\frac{-\boldsymbol{\varepsilon}_{22}^{ve}}{\tau^{ve}\dot{\boldsymbol{\varepsilon}}_{22}^{ve}}\right)\right)\right)\boldsymbol{\varepsilon}_{22}^{ve}, \tag{14}$$

where γ^{ve} is the uniaxial viscoelastic parameter. Therefore, γ^{ve} can be fitted from a pure transverse test using Eq. (14) and, thus, $\bar{\gamma}^{ve}$ in Eq. (4) can be written as a function of the uniaxial viscoelastic parameter as

$$\bar{\gamma}^{ve} = \sqrt{\gamma^{ve}\left(1 - \frac{E_{22}}{E_{11}}\nu_{12}^2\right)}. \tag{15}$$

2.2. Modelling viscoplasticity

A non-associative viscoplastic flow rule is employed allowing the volumetric viscoplastic strains and the plastic Poisson's ratios to be imposed,

$$\dot{\boldsymbol{\varepsilon}}^{vp} := \lambda\frac{\partial \varphi^p}{\partial \boldsymbol{\sigma}}, \tag{16}$$

where λ is the viscoplastic multiplier parameter and φ^p is the viscoplastic potential function. The main difference in modelling plasticity between the model developed by Cózar et al. [50,51] (elastoplastic damage model) and the one proposed in the present work is the definition of λ.

The explicit function for λ proposed by Perzyna [36], and used in many previously-developed constitutive models [38,47,48], is adopted. The overstress model [36] allows the yield function to become larger than zero for describing the viscoplastic strain. In addition, the loading–unloading hysteresis observed in the stress–strain relationships in CFRP laminates, which can be attributed to a viscoplastic behaviour of matrix rich zones [55], can be predicted from the overstress model [56]. The viscoplastic multiplier parameter is defined as

$$\lambda := \frac{\langle(\phi^p)^{1/\beta^{vp}}\rangle}{\eta^{vp}}, \tag{17}$$

where ϕ^p is the yield function, $\eta^{vp} \in (0, \infty)$ is the viscoplasticity-related parameter, β^{vp} is the rate sensitivity parameter, and $\langle x\rangle$ is the McCauley operator defined as $\langle x\rangle := (x + |x|)/2$. Then, the proposed model matches the original elastoplastic damage model with vanishing viscosity ($\eta^{vp} \to 0$) in Eq. (17) since $\dot{\boldsymbol{\varepsilon}}^{vp} \to \infty$. However, the overstress model does not reproduce the quasi-static plastic response with vanishing $\beta^{vp} \to 0$. For example, under uniaxial transverse compressive loading conditions using a quasi-static strain rate and $\beta^{vp} \to 0$, the viscoplasticity modelling produces two times the transverse compressive yield stress ($\boldsymbol{\sigma}_{22} = -2Y_{CP}$) [57]. This behaviour can be avoided by modifying Eq. (17) as in [57–59].

The yield function is defined as

$$\phi^p(\boldsymbol{\sigma}, \bar{\boldsymbol{\varepsilon}}^{vp}) := \sqrt{\left(\frac{Y_{CP} + Y_{TP}}{Y_{CP}Y_{TP}}\right)^2 \frac{\tau_t^2 + \mu_{tp}p_t^2}{1 + \mu_{tp}} + \left(\frac{\mu_{s\ell p}}{S_{LP}}\tau_\ell\right)^2} + \frac{Y_{CP} - Y_{TP}}{Y_{CP}Y_{TP}}p_t + \frac{(1 - \mu_{s\ell p})}{S_{LP}}\tau_\ell - 1 \leq 0, \tag{18}$$

where $\mu_{s\ell p}$ and μ_{tp} are viscoplastic envelope shape coefficients, Y_{CP} and Y_{TP} are the transverse compressive and tensile yield stresses, respectively, and S_{LP} is the longitudinal shear yield stress. The viscoplastic envelope shape coefficients allow the shape of the viscoplastic envelope (yield criterion) to be changed depending on the behaviour of the material. While they can be experimentally obtained, other procedures to establish them are suggested in Cózar et al. [50]. The stress invariants of Eq. (18) read

$$p_t = \frac{\boldsymbol{\sigma}_{22} + \boldsymbol{\sigma}_{33}}{2}; \tag{19}$$

$$\tau_\ell = \sqrt{\boldsymbol{\sigma}_{12}^2 + \boldsymbol{\sigma}_{13}^2}; \tag{20}$$

and

$$\tau_t = \frac{\sqrt{(\boldsymbol{\sigma}_{22} - \boldsymbol{\sigma}_{33})^2 + 4\boldsymbol{\sigma}_{23}^2}}{2}, \tag{21}$$

where $\boldsymbol{\sigma}_{ij}$ are Cartesian components of $\boldsymbol{\sigma}$.

The yield stresses in Eq. (18) are defined as a function of the equivalent viscoplastic strain ($\bar{\boldsymbol{\varepsilon}}^{vp}$) (viscoplastic internal variable). In the present work, the yield stress-equivalent viscoplastic strain relationships are defined using an experimental curve for each of them. The rate of the viscoplastic internal variable is defined as

$$\dot{\bar{\boldsymbol{\varepsilon}}}^{vp} := \sqrt{\frac{1}{2}}\left\|\dot{\boldsymbol{\varepsilon}}^{vp}\right\|. \tag{22}$$

Finally, the viscoplastic potential function is defined using Eq. (18) and by replacing the yield stresses and the viscoplastic envelope shape coefficient with the potential viscoplastic constant parameters. For example, Y_{CP} is replaced by the transverse compressive viscoplastic potential parameter ($\hat{Y}_{CP}$). These define the direction in which the viscoplastic flows and allow the viscoplastic dilatancy or contractility

to be controlled. The relationships between these potential parameters with the plastic Poisson's ratios in tension and compression (ν^p_{23C} and ν^p_{23T}, respectively) and $\nu^p_{122} := -\frac{\varepsilon^p_{22}}{\varepsilon^p_{12}}$ are defined in [50].

2.3. Modelling viscodamage

An undamaged domain, where the material response is viscoelastic and viscoplastic under complex loading states, is defined using three failure envelopes. The viscodamage activation functions associated to the longitudinal failure mechanisms are defined as

$$F_{\ell C} := \phi_{\ell C} - r_{\ell C} \leq 0, \tag{23}$$

and

$$F_{\ell T} := \phi_{\ell T} - r_{\ell T} \leq 0, \tag{24}$$

where $\phi_{\ell C}$ and $\phi_{\ell T}$ are the longitudinal compressive and tensile loading functions, respectively, and $r_{\ell C}$ and $r_{\ell T}$ are the viscoelastic threshold domains in compression and in tension, respectively. The viscodamage activation function related to the transverse failure mechanisms is defined as

$$F_t := \phi_t - 1 \leq 0, \tag{25}$$

where ϕ_t is the transverse loading functions.

The difference in the definition of $F_{\ell C}$ and $F_{\ell T}$ compared to F_t is in how the corresponding loading function is defined. The longitudinal loading functions ($\phi_{\ell C}$ and $\phi_{\ell T}$) are defined as a function of the effective stress tensor $\left(\tilde{\boldsymbol{\sigma}} = \mathbb{C}_e(d_M = 0)\boldsymbol{\varepsilon}^{ve}\right)$, whereas the transverse loading function is defined as a function of the nominal stress tensor ($\boldsymbol{\sigma}$). Therefore, the longitudinal viscoelastic domains can be explicitly obtained as

$$r_{\ell C} = \max\left(1, \max_{s\in[0,t]}\left(\phi^s_{\ell C}\right)\right), \tag{26}$$

and

$$r_{\ell T} = \max\left(1, \max_{s\in[0,t]}\left(\phi^s_{\ell T}\right)\right), \tag{27}$$

since the longitudinal loading functions only depend on the viscoelastic strain tensor. The longitudinal viscoelastic domain thresholds ($r_{\ell C}$ and $r_{\ell T}$) are the internal longitudinal viscodamage variables, are initialised equal to one, and increase with damage. However, the transverse viscodamage variables (d_t, d_{st} and $d_{s\ell}$) are the internal transverse viscodamage variables.

The loading functions proposed by Quintanas-Corominas et al. [52] are used in the present work. The main advantage of these loading functions is the option to modify the shape of the undamaged domain (failure envelopes) depending on the behaviour of the material analysed. The non-interacting maximum allowable strain criteria is employed in the longitudinal tensile as

$$\phi_{\ell T} := \frac{\boldsymbol{\varepsilon}^{ve}_{11} E_{11}}{X^v_T}, \tag{28}$$

where X^v_T is the viscous longitudinal tensile strength. The longitudinal compressive loading function reads

$$\phi_{\ell C} := \frac{1}{X^v_C}\left(\sqrt{\tilde{\boldsymbol{\sigma}}^2_{11} + \eta^q_t \tilde{p}^2_t + \eta^q_{s\ell}\tilde{\tau}^2_\ell} + \eta_t \tilde{p}_t + \eta_{s\ell}\tilde{\tau}_\ell\right), \tag{29}$$

where X^v_C is the viscous longitudinal compressive strength, and $\eta^q_t, \eta^q_{s\ell}$, η_t and $\eta_{s\ell}$ are failure envelope shape coefficients that allow the shape of the failure envelopes to be modified. The transverse loading function reads

$$\phi_t := \sqrt{\left(\frac{Y^v_C + Y^v_T}{Y^v_T Y^v_C}\right)^2 \frac{\tau^2_t + \mu_t p^2_t}{1+\mu_t} + \left(\frac{\mu_{s\ell}}{S^v_L}\tau_\ell\right)^2} + \frac{Y^v_C - Y^v_T}{Y^v_T Y^v_C} p_t + \frac{(1-\mu_{s\ell})}{S^v_L}\tau_\ell, \tag{30}$$

where Y^v_C and Y^v_T are the viscous transverse compressive and tensile strengths, respectively, S^v_L is the viscous longitudinal shear strength, and μ_t and τ_ℓ are failure envelope shape coefficients. The strengths in Eqs. (28)–(30) can be defined by considering the dynamic effects using experimental expressions as a function of: strain rate [19,38–45], viscoplastic strains as in metallic material models [60,61], strain rate, and ultimate strain as in concrete constitutive models [62], etc.

The softening law of each transverse viscodamage variable is defined in the equivalent viscoelastic domain to simplify the implementation. The stress tensor in Eq. (13) can be rewritten as

$$\boldsymbol{\sigma} = \mathbb{C}_e \bar{\boldsymbol{\varepsilon}}^{ve}, \tag{31}$$

where the equivalent viscoelastic strain tensor yields

$$\bar{\boldsymbol{\varepsilon}}^{ve} = \boldsymbol{\varepsilon}^{ve} + \mathbb{H}\boldsymbol{\Gamma}\mathbb{C}_e\boldsymbol{\Gamma}(\boldsymbol{\varepsilon}^{ve} - \boldsymbol{\varepsilon}^i). \tag{32}$$

Therefore, the definition of the viscodamage evolution functions match that of the quasi-static constitutive model since Eq. (31) has the same form to the quasi-static model ($\boldsymbol{\sigma} = \mathbb{C}_e\boldsymbol{\varepsilon}^e$) replacing $\bar{\boldsymbol{\varepsilon}}^{ve}$ by $\boldsymbol{\varepsilon}^e$. Additionally, the softening laws follow the same shape in the proposed domain ($\bar{\boldsymbol{\varepsilon}}^{ve}$) instead of the $\boldsymbol{\varepsilon}^{ve}$ domain. However, the amount of mechanical energy dissipated by viscodamage is guaranteed in the $\boldsymbol{\varepsilon}^{ve}$ domain and calibrated with the corresponding fracture toughness.

The outcome of this simplification on the softening response is analysed in Fig. 4, and no significant effect is observed. The transverse viscodamage variables can be explicitly obtained following the approach presented in [51]. The relationship of the longitudinal viscodamage variables with the corresponding viscoelastic threshold domain is described in [50]. The fracture toughness can be also defined as a function of the strain rate also using experimental expressions. Finally, a bilinear softening law is defined for the longitudinal direction and a linear softening law in the directions governed by the matrix.

3. Results

Several tests are performed to demonstrate the capabilities of the proposed constitutive model at the Gauss-point level. In addition, the off-axis compressive experimental tests carried out by Koerber et al. [15] are used to demonstrate the ability of the present model to predict the inelastic deformation and fracture of CFRPs under different loading rates. In both cases, the IM7/8552 unidirectional prepreg system is employed with the quasi-static model input parameters listed in Table 2. Most of these parameters can be measured or fitted directly from experimental tests. However, there is no experimental test for determining ν^p_{122}. In the present work, ν^p_{122} is defined by assuming no volumetric plastic strains. Additionally, there are no tests to determine the shape of the failure envelopes. Here, the shape of the failure envelopes is fitted from the 3D failure criteria proposed by [63]. New methodologies are needed to analyse the mechanical behaviour of CFRPs under multi-axial loading conditions [64].

The dynamic model input parameters are listed in Table 3 and their calibration is explained in detail in Section 3.3. Note that, only four dynamic parameters are required in the viscoelastic and viscoplastic regions due to the isotropy of the CFRP laminates in the directions governed by the matrix.

3.1. Calibration of the strengths under dynamic conditions

Based on the experimental observations reported in the literature, the longitudinal and transverse strengths of CFRPs are strain-rate dependent. There is no significant experimental evidence of how to define the evolution of the strengths due to high strain rates for the selected material system (IM7/8552). As such, the expression proposed by Wiegand [78] and calibrated for the selected material in [16,19] is used. Therefore, the dynamic strengths are defined as

$$\sigma^{dyn}_u := \sigma_u\left(1 + (1.13\times10^{-4}\dot{\boldsymbol{\varepsilon}}^{ve}_{ij})^{\frac{1}{4}}\right), \tag{33}$$

Table 2
Quasi-static model input parameters for the IM7/8552 unidirectional prepreg system. Note that the suggested tests do not need to match the tests that were performed to obtain the values of the properties.

	Symbol	Value	Unit	Source	Test
	Density	1570	kg/m^3	[65]	Test method for density of plastics [66,67]
Elastic	E_{11}	171 420.00	MPa	[68]	Longitudinal tensile test (ASTM D3039) [69]
	E_{22}	9080.00	MPa	[68]	Transverse tensile test (ASTM D3039) [69]
	G_{12}	5290.00	MPa	[68]	Longitudinal shear tensile test (ASTM D3518) [70]
	ν_{12}	0.32	–	[68]	Longitudinal tensile test (ASTM D3039) [69]
	ν_{23}	0.45[a]	–	[50]	Transverse test [71]
Plastic	$Y_{CP}(\bar{\varepsilon}^p)$	curve		[72]	Transverse compressive test (ASTM D6641) [73][b]
	$Y_{TP}(\bar{\varepsilon}^p)$	curve		[72]	Transverse tensile test (ASTM D3039) [69][b]
	$S_{LP}(\bar{\varepsilon}^p)$	curve		[72]	Longitudinal shear tensile test (ASTM D3518) [70][b]
	μ_{tp}	0.47[a]	–	[50]	Multiaxial test
	$\mu_{s\ell p}$	1.00[a]	–	[50]	Multiaxial test
	ν^p_{23T}	1.00[a]	–	[72]	Transverse test [71]
	ν^p_{23C}	1.00[a]	–	[72]	Transverse test [71]
	ν^p_{122}	0.00[a]	–	[72]	–
Damage	X_C	1017.50	MPa	[74]	Longitudinal compressive test (ASTM D6641) [73]
	$f_{X_C} X_C$	203.50	MPa	[52]	Compact compressive test [75]
	$f_{\mathcal{G}_{X_C}} \mathcal{G}_{X_C}$	26.58	N/mm	[52]	Compact compressive test [75]
	X_T	2323.50	MPa	[74]	Longitudinal tensile test (ASTM D3039) [69]
	$f_{X_T} X_T$	464.70	MPa	[52]	Compact tensile test [75]
	$\mathcal{G}_{X_T}$	97.80	N/mm	[76]	Compact tensile test [75]
	$f_{\mathcal{G}_{X_T}} \mathcal{G}_{X_T}$	48.90	N/mm	[52]	Compact tensile test [75]
	Y_C	253.70	MPa	[52]	Transverse compressive test (ASTM D6641) [73]
	$\mathcal{G}_{Y_C}$	2.8[a]	N/mm	[51]	–
	Y_T	62.30	MPa	[68]	Transverse tensile test (ASTM D3039) [69]
	$\mathcal{G}_{Y_T}$	0.28	N/mm	[68]	Double cantilever beam test [77][c]
	S_L	92.30	MPa	[68]	Longitudinal shear tensile test (ASTM D3518) [70]
	$\mathcal{G}_{S_L}$	0.80	N/mm	[68]	4-point bending end notched test (ASTM D5528) [77][c]
	μ_t	0.90[a]	–	[52]	Multiaxial test
	$\mu_{s\ell}$	1.00[a]	–	[52]	Multiaxial test
	$\eta_{s\ell}$	9.50[a]	–	[52]	Multiaxial test
	$\eta^q_{s\ell}$	0.00[a]	–	[52]	Multiaxial test
	η_t	12.00[a]	–	[52]	Multiaxial test
	η^q_t	350.00[a]	–	[52]	Multiaxial test

[a] Adjusted or assumed.
[b] Assuming no damage occurs until the specimen fails, the plastic strain can then be calculated by subtracting the elastic strain, as the ratio of stress to elastic modulus, from the total strain.
[c] Assuming that the intralaminar fracture toughness is equivalent to the interlaminar fracture toughness.

Table 3
Dynamic model input parameters for the IM7/8552 unidirectional prepreg system.

	Symbol	Value	Unit
Viscoelastic	γ^{ve}	0.35	–
	τ^{ve}	10^{-4}	s
Viscoplastic	β^{vp}	1.00	–
	η^{vp}	2.25×10^{-5}	s
Viscodamage	η^{vd}	4.00×10^{-5}	s

where σ_u is the strength under quasi-static loading conditions (e.g. the longitudinal compressive strength is $\sigma_u^{dyn}(\sigma_u = X_C) = X_C^{dyn}$). Eq. (33) is proposed for a 1D state, thus Eq. (33) must be extended to a 3D state to be employed in the present constitutive model. Eq. (33) is a function of a scalar value related to the viscoelastic strain rate ($\dot{\varepsilon}^{ve}_{ij}$) and must be extended to account for the viscoelastic strain rate tensor ($\dot{\boldsymbol{\varepsilon}}^{ve}$). The extension is carried out by defining a new norm to evaluate Eq. (33) under 3D loading conditions. In the longitudinal compressive direction, the strength norm is defined as

$$\dot{\phi}^{qs}_{\ell C} := \frac{d\phi^{qs}_{\ell C}}{d\boldsymbol{\varepsilon}^{ve}}\dot{\boldsymbol{\varepsilon}}^{ve}, \tag{34}$$

where $\phi^{qs}_{\ell C}$ is the longitudinal compressive loading function defined in Eq. (29) and evaluated by replacing X^v_C with X_C (the static longitudinal compressive strength). Therefore, dynamic longitudinal compressive strength (X_C^{dyn}) can be obtained by evaluating Eq. (34) under uniaxial longitudinal compressive conditions (as with Eq. (33) was obtained). Therefore, the dynamic longitudinal compressive strength yields

$$X_C^{dyn} = X_C\left(1 + \left(1.13\times10^{-4}\frac{\dot{\phi}^{qs}_{\ell C}X_C}{E_{11}}\right)^{\frac{1}{4}}\right). \tag{35}$$

The norm to obtain the transverse strengths is defined as

$$\dot{\phi}^{qs}_t := \frac{d\phi^{qs}_t}{d\boldsymbol{\varepsilon}^{ve}}\dot{\boldsymbol{\varepsilon}}^{ve}, \tag{36}$$

where ϕ^{qs}_t is the transverse loading function defined in Eq. (30) with $d_M = 0$ and evaluated by replacing the viscous strengths with the quasi-static strengths. The dynamic strengths are then obtained by evaluating Eq. (36) with uniaxial conditions; like Eq. (33) was obtained for the corresponding strength. For instance, the dynamic transverse compressive strength (Y_C^{dyn}) is obtained by evaluating Eq. (36) under pure transverse compressive conditions,

$$Y_C^{dyn} = Y_C\left(1 + \left(1.13\times10^{-4}\frac{\dot{\phi}^{qs}_t Y_C}{E_{22}}\right)^{\frac{1}{4}}\right). \tag{37}$$

The rest of transverse dynamic strengths read

$$Y_T^{dyn} = Y_T\left(1 + \left(1.13\times10^{-4}\frac{\dot{\phi}^{qs}_t Y_T}{E_{22}}\right)^{\frac{1}{4}}\right), \tag{38}$$

and,

$$S_L^{dyn} = S_L\left(1+\left(1.13\times10^{-4}\frac{\dot{\phi}_t^{qs}S_L}{G_{12}}\right)^{\frac{1}{4}}\right). \tag{39}$$

Explicit FE solver is used to obtain the numerical predictions, and both norms ($\dot{\phi}_{\ell C}^{qs}$ and $\dot{\phi}_t^{qs}$) are numerically integrated using the backward Euler method. No significant error is found in the numerical integration process of $\dot{\phi}_{\ell C}^{qs}$ and $\dot{\phi}_t^{qs}$ since the increment of the time in the explicit FE solver is less than 10^{-8} s.

In the present work, the longitudinal tensile strength is defined strain rate-independent since no experimental data on the strength-strain rate relationship are available for the selected material. As with the longitudinal tensile strength, the fracture toughnesses are defined constants since no clear trend or experimental data were found.

A viscosity regularisation of the strengths is considered to prevent high strength rates with high strain rate. The viscous strength rate is defined as

$$\dot{\sigma}_u^v := \frac{\sigma_u^{dyn}-\sigma_u^v}{\eta^{vd}}, \tag{40}$$

where η^{vd} is a viscodamage-related parameter. This viscous regularisation is applied at all strengths defined in Eqs. (29) and (30). For example, the viscous longitudinal compressive strength (X_C^v) is obtained using Eq. (35) and its viscous regularisation ($\dot{\sigma}_u^v(\sigma_u^{dyn}=X_C^{dyn})=\dot{X}_C^v$) is then applied based on Eq. (40).

3.2. Gauss-point level tests

Virtual tests at the Gauss-point level are carried out to verify that the present constitutive model complies with the assumptions made in its development (see Section 2). A single Gauss-point is loaded under simple longitudinal shear conditions (see Fig. 4a) at a high loading rate ($\dot{\varepsilon}_{12}=200\ s^{-1}$), as well as at a quasi-static loading rate ($\dot{\varepsilon}_{12}=10^{-4}\ s^{-1}$). The Gauss-point is defined as a cube of 0.24 mm × 0.24 mm × 0.24 mm (the same in-plane mesh element size is used in the off-axis compressive FE models of Section 3.3).

The schematic representation of the deformed shape of the simple longitudinal shear test is presented in Fig. 4b. The stress–strain response obtained from the high strain rate in the viscoelastic region is stiffer than that obtained from the quasi-static loading rate conditions, see Fig. 4c. The stress component from the Maxwell element in that region is linear since τ^{ve} of the selected material is large enough compared to the time when the viscoplastic process starts ($\tau^{ve}\gg 2.10\times10^{-5}$ s). The viscoplastic hardening from the dynamic case starts with a smaller ε_{12} compared to the quasi-static simulation, but at similar σ_{12} (see cross markers in Fig. 4c). Furthermore, the hardening process is also stiffer at the high strain rate; this can be observed by comparing the two responses with no damage ($d_{st}=0$) in Fig. 4c. This indicates a high strain rate dependency of the analysed material on both the viscoelastic and viscoplastic hardening processes under simple longitudinal shear loading conditions.

The increase in the strength with the high strain rate obtained from Eq. (39) ($S_L^{dyn}=128.09$ MPa at $\dot{\varepsilon}_{12}=200\ s^{-1}$) is properly predicted from the dynamic simulation in Fig. 4c. Equivalent energy dissipated by the viscodamage process is obtained from both loading rate conditions (0.8 N/mm, grey area in Fig. 4c) since the fracture toughness is defined as strain rate-independent for the selected material and which match $\mathcal{G}_{S_L}$. Therefore, the absolute value of the slope of the softening law increases with a high strain rate.

The effect of implementing the equivalent viscoelastic domain (see Eq. (31)) on the viscodamage softening response is analysed using a linear regression analysis in the softening region. Although the softening is not a straight line due to the non-linearities contributed by the Maxwell element, this is not significant. The coefficient of determination from the linear regression analysis conducted in the viscodamage softening region is equal to one ($R^2=1.00$, linear stress–strain relationship in the viscodamage softening).

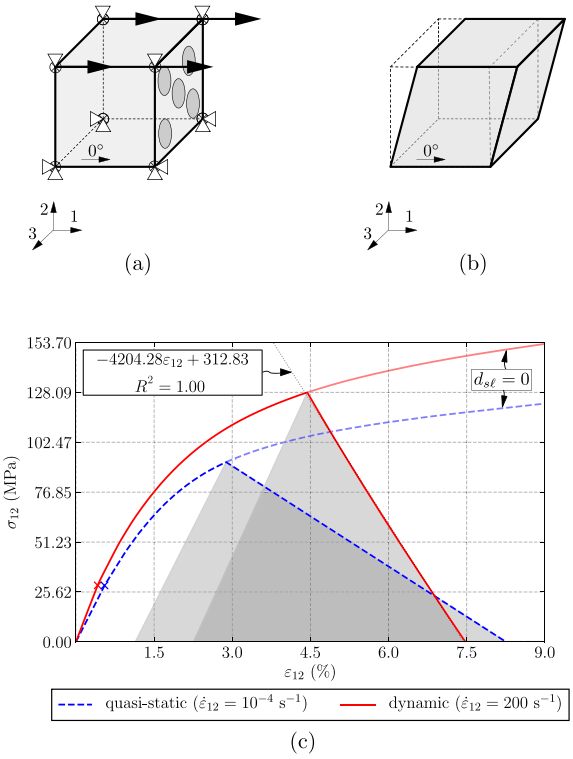

Fig. 4. Simple longitudinal shear virtual test at the Gauss-point level at two different strain rate conditions: (a) boundary conditions, (b) deformed shape, and (c) stress vs. strain curve. The cross markers in the stress–strain curve represent when the viscoplastic process starts. The dotted black straight line in the stress–strain curve represents the linear regression analysis curve applied to the viscodamage softening behaviour of the dynamic response, and the grey areas refer to the energy dissipated by viscodamage.

A relaxation test is also carried out applying simple longitudinal shear loading conditions. A Gauss-point is loaded to a prescribed strain ($\varepsilon_{12}=4\%$) at $\dot{\varepsilon}_{12}=200\ s^{-1}$ and, then maintained it loaded at $\dot{\varepsilon}_{12}=0$ over a long period of time, see Fig. 5a. In this case, a time-dependent response is observed. Firstly, the nominal longitudinal shear stress (σ_{12}) increases with the increasing of ε_{12}. Then, ε_{12} remains constant and σ_{12} slowly decreases since the stress component of the Maxwell element decreases and the viscoplastic process relaxes until they vanish, see Fig. 5b. Finally, the material is damaged without increasing ε_{12} but due to how S_L^v is relaxed. The viscodamage variable $d_{s\ell}$ is activated after ε_{12} is fixed since S_L^v relaxes faster than σ_{12}. Therefore, σ_{12} decreases at the end of the test not only because the material relaxes, but also because a failure mechanism is initiated ($d_{s\ell}>0$). Note that, less than 30% of $\mathcal{G}_{S_L}$ is dissipated during the relaxation test. In addition, the longitudinal shear strength is also strain rate-dependent and its viscous regularisation is observed in Fig. 5b; S_L^v tends to S_L at the end of the test.

The stress–strain relationship obtained from the relaxation case until to fix $\varepsilon_{12}=4\%$ matches the one obtained from the monotonic virtual test under simple longitudinal shear conditions at high strain rate, see Fig. 6. However, although the stress vertically drops during the relaxation step, but does not reach the stress from the quasi-static test at $\varepsilon_{12}=4\%$. In both cases (quasi-static and relaxation tests), the stress remains constant at $\sigma_{12}=(1-d_{s\ell})E_{12}\varepsilon_{22}^{ve}$ but with different viscoplastic and viscodamage states due to how the material was loaded over time.

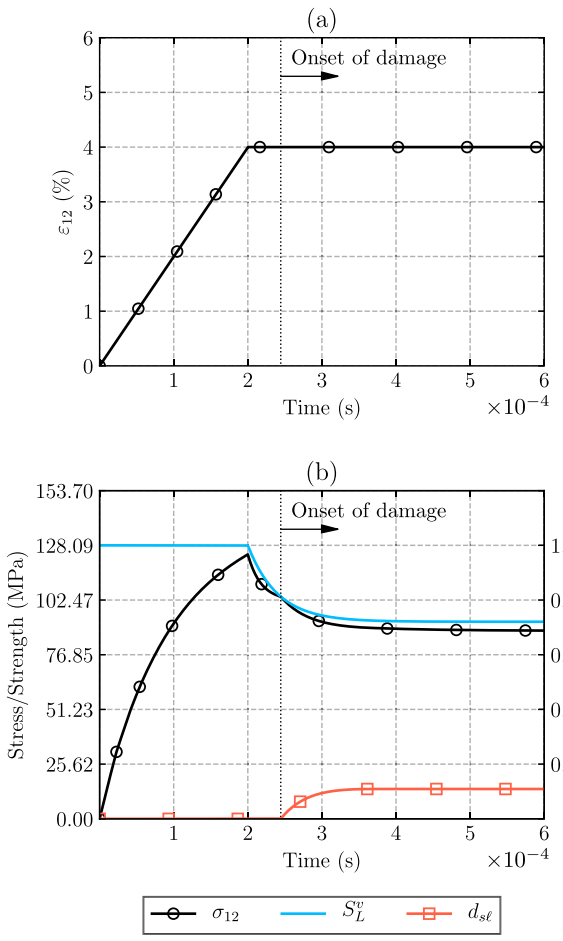

Fig. 5. Relaxation virtual test under simple longitudinal shear loading conditions at the Gauss-point level: (a) strain applied and (b) nominal longitudinal shear stress, evolution of the longitudinal shear strength and viscodamage variable.

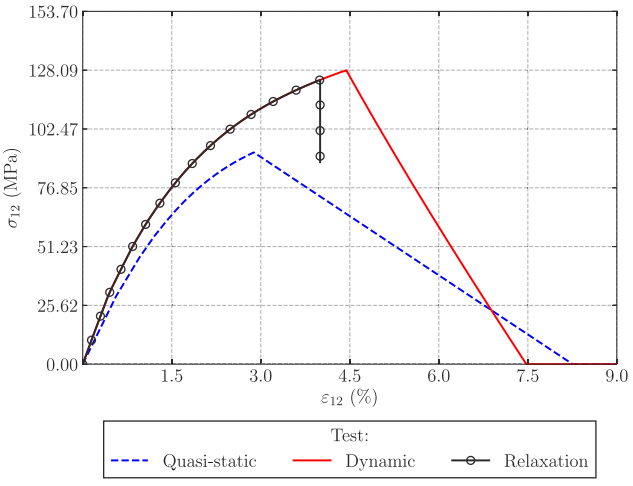

Fig. 6. Comparison of the simple longitudinal shear virtual tests from the relaxation test and monotonically increasing tests.

3.3. Off-axis tests

The mechanical response of the off-axis compressive tests carried out by Koerber et al. [15] under different loading rates with the fibre angle orientation $\theta = 15°, 30°, 45°, 60°, 75°$ and $90°$ is predicted using FE models. The present constitutive model is implemented in a user material subroutine (VUMAT) and the Abaqus/Explicit solver [79] is used to obtain the finite element results, employing 3D eight-node C3D8R solid elements with reduced integration. The in-plane element size is defined equal to 0.24 mm to prevent the snap-back of the constitutive softening laws for each failure mechanism [80]. In addition, three elements through-the-thickness of each ply are used.

The in-plane dimensions of the specimens are 10 mm × 20 mm and the laminates have a 32-ply thickness. Vertical displacement is applied on the top face of the FE models, while the bottom face is fixed in this direction, see Fig. 7a. The quasi-static FE simulations are performed applying the vertical displacement at constant low velocity to prevent kinetic effects. However, the loading rates applied during the dynamic experimental tests are also employed in the dynamic simulations, see Fig. 7b. In addition, the remaining boundary conditions shown in Fig. 7a are defined to prevent rigid body motions.

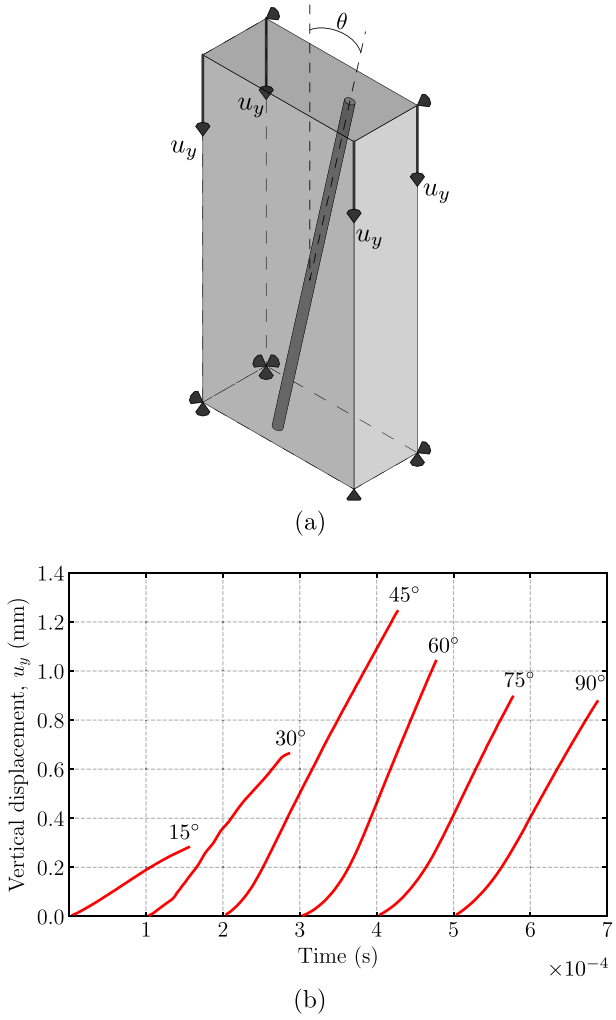

Fig. 7. Schematic representation of the boundary conditions (a), and the displacement–time curves applied to the dynamic tests in the off-axis compressive tests [15] (b).

Because no experimental data were found in the literature, the dynamic model input parameters summarised in Table 3 are fitted by tuning these parameters. Eq. (14) cannot be employed with the experimental data measured from [15] since the loading rate in the elastic region is not constant, see the first sections of the curves in Fig. 7b. The 45° dynamic test is used to compare the numerical stress–strain curve with those experimentally obtained since the highest

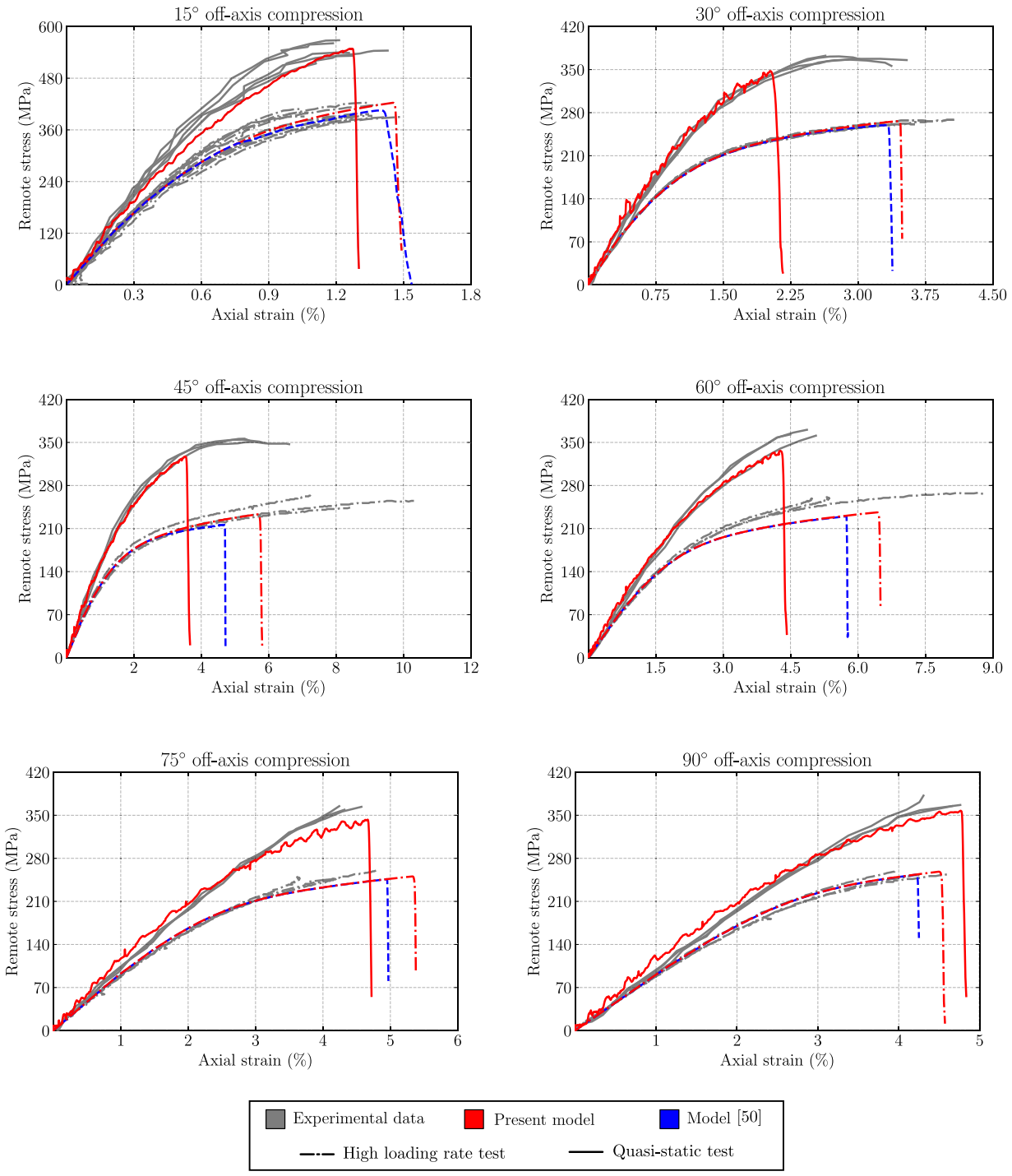

Fig. 8. Numerical–experimental comparison of the remote stress vs. axial strain curves of the off-axis compressive tests performed by Koerber et al. [15].

experimental ultimate strain was obtained from this test. Firstly, the viscoelastic input parameters (τ^{ve}, γ^{ve}) are varied with pure viscoelastic FE response (the viscoplastic and viscodamage model are disabled in this step) to properly capture the initial slope of the experimental data. Then, the viscoplastic parameters (β^{vp}, η^{vp}) are fitted using the fully constitutive model to reproduce the hardening response. Finally, the viscodamage-related parameter (η^{vd}) is set equal to 4.00×10^{-5}. The effect of η^{vd} on the failure strength is not significant since the loading rate is almost constant when the specimen fails and this stabilisation time is large enough compared with η^{vd}, see Fig. 7b.

The stress vs. strain curves from the present constitutive model and the strain rate-independent constitutive model [50] are compared with the experimental data [15] in Fig. 8. The initial slope of the dynamic tests are properly predicted from the present constitutive model for $\theta = 15°, 30°, 45°$ and $60°$ and a slightly stiffer elastic response is observed for $\theta = 75°$ and $90°$. The hardening response of the dynamic simulations is in good agreement with the experimental data. Furthermore, the failure strength of the specimens from the high strain rate numerical models is also in good agreement with the experimental data, with its highest relative error being less than 7.81% for $\theta = 60°$. Furthermore, good agreement is found in the ultimate strain between the numerical and experimental dynamic results except for $\theta = 30°$ and $45°$ in which a small change in stress produces a significant increase in axial strain.

The quasi-static numerical results from the compressive off-axis tests are also compared with the corresponding experimental data. The elastic and hardening response are properly predicted from the present constitutive model. In addition, the numerical failure strength of the specimens is also in good agreement with the experimental data, albeit except for $\theta = 45°$ and $60°$. Similar predictions are obtained from the strain rate-independent constitutive model [50]. The failure strength predictions in the quasi-static results can be improved by experimentally measuring S_L [50]. This material property has a significant influence on the $\sigma_{22}-\sigma_{12}$ stress space of the failure envelope and is not experimentally obtained in the present work. S_L is assumed from an in-plane shear test following the ASTM D 3518/3518M-94 test standard [70], and thus S_L is estimated when 5% of the axial strain is reached. Note that, the present constitutive model overpredicts the failure strength from the quasi-static tests compared to those obtained from the model [50]. This is due to using the definition of the material strengths as a function of the strain rate as described by Eq. (33).

4. Conclusions

A 3D constitutive model is proposed to account for the strain rate dependence of the stress–strain response of carbon fibre-reinforced polymer (CFRP) laminates. The proposed constitutive model is based on a previous strain rate-independent model and is extended to account for the strain rate effects. The generalised Maxwell model is employed to predict the viscoelastic response under dynamic loading conditions. An overstress model is used to account for the viscoplastic strains of CFRPs. In addition, a new viscodamage model is proposed to account for the onset of damage as well as its propagation under different loading rates. The viscodamage modelling is based on a quasi-static damage model and is extended to dynamic conditions using experimental strength-strain rate relationships. In addition, the objectivity of the viscodamage model is ensured by regularising the viscodamage energy dissipated with the characteristic element size.

The proposed constitutive model is linked with a finite element solver to show its predictive capabilities. The constitutive model is able to reproduce the stiffer stress–strain response of CFRPs under high strain rates. In addition, the response of a relaxation test shows how the material relaxes and how the onset and propagation of the viscodamage occur without increasing the strains, since the strength relaxes faster than the stresses.

Numerical–experimental comparison of off-axis compressive tests at different loading rates is also carried out to demonstrate the ability of the proposed constitutive model to predict the mechanical response of CFRP laminates. The comparison of the dynamic tests shows good agreement in the viscoelastic, viscoplastic and viscodamage regions. In addition, quasi-static tests are properly predicted by the proposed constitutive model and are in good agreement with the previously strain rate-independent model. Further experimental investigations are required to better understand the onset of failure and its propagation under dynamic loading conditions, but also to quantify the dissipated energy converted to heat to cross-validate the dissipated energy predicted by the model.

CRediT authorship contribution statement

I.R. Cózar: Conceptualization, Methodology, Validation, Formal analysis, Investigation, Writing – original draft, Writing – review & editing. **P. Maimí:** Conceptualization, Methodology, Validation, Formal analysis, Investigation, Writing – review & editing, Supervision. **E.V. González:** Conceptualization, Methodology, Validation, Formal analysis, Investigation, Writing – review & editing, Supervision. **P.P. Camanho:** Formal analysis, Investigation, Writing – review & editing, Supervision. **F. Otero:** Conceptualization, Methodology, Validation, Formal analysis, Investigation, Writing – review & editing, Supervision.

Declaration of competing interest

The authors declare the following financial interests/personal relationships which may be considered as potential competing interests: Emilio Gonzalez reports financial support was provided by European Commission. Ivan Cozar reports financial support was provided by Agència de gestió d'ajuts universitaris i de recerca govern de Catalunya.

Data availability

No data was used for the research described in the article.

Acknowledgements

The first author would like to acknowledge the support of the Catalan Government (Agència de Gestió d'Ajuts Universitaris i de Recerca) through Grant 2019FI_B_01117. The present research project has received funding from the Clean Sky 2 Joint Undertaking (JU) under grant agreements No. 886519 (BEDYN). The JU receives support from the European Union's Horizon 2020 Research and Innovation programme and the Clean Sky 2 JU members other than the Union. The authors would also like to express special thanks to the Topic Managers of said European project for their support in the development of the work presented: Dassault Aviation. Grant PID2022-137979OB-I00 funded by MICIU/AEI/10.13039/501100011033 and by FEDER-European Union. Open Access funding provided thanks to the CRUE-CSIC agreement with Elsevier.

Appendix. Thermodynamic consistency of the viscoelastic-viscoplastic viscodamage model

The demonstration of the thermodynamic consistency of the viscoelastic–viscoplastic viscodamage model is presented in this section. To ensure the thermodynamically irreversibility of dissipation processes, the energy dissipated must be positive or at least null. The mechanical energy dissipated of the constitutive model presented in Section 2 can be rewritten from Eq. (10) as

$$\Xi = -\frac{\partial \Psi}{\partial \boldsymbol{\varepsilon}^i}\dot{\boldsymbol{\varepsilon}}^i - \frac{\partial \Psi}{\partial \boldsymbol{\varepsilon}^{vp}}\dot{\boldsymbol{\varepsilon}}^{vp} - \sum_M \frac{\partial \Psi}{\partial d_M}\dot{d}_M \geq 0. \tag{A.1}$$

Then, if each term in Eq. (A.1) is equal to or greater than zero, the thermodynamic irreversibility of dissipation processes will be ensured. The following subsections of this appendix describe the demonstration that the constitutive model presented in Section 2 fulfils the inequality in Eq. (A.1).

A.1. Thermodynamic consistency of the viscoelastic energy dissipated

The mechanical energy dissipated due to a viscoelastic process from Eq. (A.1) reads

$$-\frac{\partial \Psi}{\partial \boldsymbol{\varepsilon}^i}\dot{\boldsymbol{\varepsilon}}^i = \left(\mathbb{C}_{ve}(\boldsymbol{\varepsilon} - \boldsymbol{\varepsilon}^{vp} - \boldsymbol{\varepsilon}^i)\right)^T \dot{\boldsymbol{\varepsilon}}^i, \tag{A.2}$$

where $\partial_{\varepsilon^i}(\Psi)$ is the stress tensor of the Hookean element of the Maxwell component (bottom left branch in Fig. 2, left hand side of Eq. (5)). Therefore, by introducing the right hand side of Eq. (5) into Eq. (A.2), the viscoelastic mechanical energy dissipated yields

$$-\frac{\partial \Psi}{\partial \boldsymbol{\varepsilon}^i}\dot{\boldsymbol{\varepsilon}}^i = (\boldsymbol{\Gamma}\mathbb{C}_e\boldsymbol{\Gamma}\mathbb{T}^{ve}\dot{\boldsymbol{\varepsilon}}^i)^T\dot{\boldsymbol{\varepsilon}}^i. \tag{A.3}$$

The non-negativity of $\mathbb{C}_e$ can be demonstrate by the definition of $\mathbb{H}$, since the inverse of a positive semi-definite matrix is also a positive semi-definite matrix [81]. Therefore, the non-negativity of $\mathbb{H}$ can be demonstrate by the product of an arbitrary vector $(\boldsymbol{\sigma})$ with $\mathbb{H}$ [81], as

$$\boldsymbol{\sigma}^T\mathbb{H}\boldsymbol{\sigma} = \frac{\sigma_\ell^2}{(1-d_\ell)E_{11}} - \frac{4\nu_{12}\sigma_\ell p_t}{E_{11}}$$

$$+\frac{p_t^2}{(1-d_t)E_t}+\frac{\tau_t^2}{(1-d_{st})G_t}+\frac{\tau_\ell^2}{(1-d_{s\ell})G_{12}}. \tag{A.4}$$

Applying the thermodynamic restrictions of the elastic material properties of transversely isotropic materials [82],

$$\begin{aligned} &E_{11},E_{22},G_{12}>0\\ &|\nu_{23}|<1\\ &|\nu_{12}|<\sqrt{\frac{E_{11}}{E_{22}}}\\ &-1<\nu_{23}<1-2\nu_{12}^2\frac{E_{11}}{E_{22}}, \end{aligned} \tag{A.5}$$

and by setting the range of the damage variables to $d_M \in [0,1]$, the expression in Eq. (A.4) is always non-negative,

$$\boldsymbol{\sigma}^T\mathbb{H}\boldsymbol{\sigma}\geq 0. \tag{A.6}$$

Therefore, $\mathbb{H}$ is a positive semi-definite matrix and its inverse matrix ($\mathbb{C}_e$) is also a positive semi-definite matrix.

The non-negativity of $\boldsymbol{\Gamma}\mathbb{C}_e\boldsymbol{\Gamma}\mathbb{T}^{ve}$ can be demonstrated because the product of positive semi-definite matrices is equal to its transpose thereby resulting also in a positive semi-definite matrix,

$$\tau^{ve}\bar{\gamma}^{ve2}\mathbb{I}^{ve}\mathbb{C}_e\mathbb{I}^{ve}=\tau^{ve}\bar{\gamma}^{ve2}(\mathbb{I}^{ve}\mathbb{C}_e\mathbb{I}^{ve})^T. \tag{A.7}$$

Therefore, $\boldsymbol{\Gamma}\mathbb{C}_e\boldsymbol{\Gamma}\mathbb{T}^{ve}$ is a positive semi-definite matrix for all $\tau^{ve}\geq 0$. Finally, Eq. (A.3) can be rewritten as

$$-\frac{\partial\Psi}{\partial\boldsymbol{\varepsilon}^i}\dot{\boldsymbol{\varepsilon}}^i=\dot{\boldsymbol{\varepsilon}}^{iT}(\boldsymbol{\Gamma}\mathbb{C}_e\boldsymbol{\Gamma}\mathbb{T}^{ve})^T\dot{\boldsymbol{\varepsilon}}^i, \tag{A.8}$$

where the right hand side of Eq. (A.8) yields the condition of the product of a positive semi-definite matrix by a non-negative vector ($\dot{\boldsymbol{\varepsilon}}^i$) [81]. Hence, the mechanical energy dissipated due to a viscoelastic process is always positive or at least null.

A.2. Thermodynamic consistency of the viscoplastic energy dissipated

The mechanical energy dissipated due to a viscoplastic process from Eq. (A.1) yields

$$-\frac{\partial\Psi}{\partial\boldsymbol{\varepsilon}^{vp}}\dot{\boldsymbol{\varepsilon}}^{vp}=\left(\mathbb{C}_e(\boldsymbol{\varepsilon}-\boldsymbol{\varepsilon}^{vp})+\mathbb{C}_{ve}(\boldsymbol{\varepsilon}-\boldsymbol{\varepsilon}^{vp}-\boldsymbol{\varepsilon}^i)\right)^T\dot{\boldsymbol{\varepsilon}}^{vp}. \tag{A.9}$$

Then, Eq. (A.9) can be rewritten by inserting Eq. (13) and Eq. (16) as

$$-\frac{\partial\Psi}{\partial\boldsymbol{\varepsilon}^{vp}}\dot{\boldsymbol{\varepsilon}}^{vp}=\lambda\boldsymbol{\sigma}^T\frac{\partial\varphi^p}{\partial\boldsymbol{\sigma}}. \tag{A.10}$$

Therefore, the mechanical energy dissipated of Eq. (A.9) yields

$$\begin{aligned} -\frac{\partial\Psi}{\partial\boldsymbol{\varepsilon}^{vp}}\dot{\boldsymbol{\varepsilon}}^{vp}=\lambda\Bigg(&\sqrt{\left(\frac{\hat{Y}_{CP}+\hat{Y}_{TP}}{\hat{Y}_{TP}\hat{Y}_{CP}}\right)^2\frac{\tau_t^2+\hat{\mu}_{tp}p_t^2}{1+\hat{\mu}_{tp}}+\left(\frac{\hat{\mu}_{s\ell p}}{\hat{S}_{LP}}\tau_\ell\right)^2}\\ &+\frac{\hat{Y}_{CP}-\hat{Y}_{TP}}{\hat{Y}_{TP}\hat{Y}_{CP}}p_t+\frac{(1-\hat{\mu}_{s\ell p})}{\hat{S}_{LP}}\tau_\ell\Bigg). \end{aligned} \tag{A.11}$$

Hence, the first and third terms in parenthesis of Eq. (A.11) will always be non-negative for all $\hat{\mu}_{s\ell p}\leq 1$. Then, the right hand side of Eq. (A.11) only will be negative if $p_t<0$, since $\lambda\geq 0$ from the Kuhn–Tucker conditions and all viscoplastic potential parameter must be defined positive. The worst case scenario to meet the negativity of the mechanical energy dissipated due to a viscoplastic process is

$$\begin{aligned} &\boldsymbol{\sigma}_{23}=\boldsymbol{\sigma}_{13}=\boldsymbol{\sigma}_{12}=0\\ &\boldsymbol{\sigma}_{22}=\boldsymbol{\sigma}_{33}<0. \end{aligned} \tag{A.12}$$

Hence, by introducing the conditions of Eq. (A.12) in Eq. (A.11), the viscoplastic mechanical energy dissipated yields

$$\left(-\frac{\partial\Psi}{\partial\boldsymbol{\varepsilon}^{vp}}\dot{\boldsymbol{\varepsilon}}^{vp}\right)\Big|_{Eq.\ (A.12)}=\frac{\lambda}{\hat{Y}_{TP}\hat{Y}_{CP}}\left((\hat{Y}_{CP}+\hat{Y}_{TP})\sqrt{\frac{\hat{\mu}_{tp}}{1+\hat{\mu}_{tp}}}-(\hat{Y}_{CP}-\hat{Y}_{TP})\right)|p_t|. \tag{A.13}$$

Therefore, the following conditions are imposed to ensure the non-negativity of the mechanical energy dissipated by a viscoplastic process:

$$\begin{aligned} &\hat{\mu}_{s\ell p}\leq 1\\ &\hat{Y}_{TP}\leq\hat{Y}_{CP}\\ &\frac{1+\frac{\hat{\mu}_{tp}}{1+\hat{\mu}_{tp}}}{1-\frac{\hat{\mu}_{tp}}{1+\hat{\mu}_{tp}}}\leq\frac{\hat{Y}_{CP}}{\hat{Y}_{TP}}. \end{aligned} \tag{A.14}$$

A.3. Thermodynamic consistency of the viscodamage energy dissipated

The mechanical energy dissipated due to a viscodamage process defined in Eq. (A.1) can be rewritten knowing that $\mathbb{C}_e(d_M)$ (its inverse is defined in Eq. (6)) and applying the corresponding chain rule as

$$\begin{aligned} -\sum_M\frac{\partial\Psi}{\partial d_M}\dot{d}_M=-\frac{1}{2}\Bigg(&(\boldsymbol{\varepsilon}-\boldsymbol{\varepsilon}^{vp})^T\sum_M\left(\frac{\partial\mathbb{C}_e}{\partial d_M}\dot{d}_M\right)(\boldsymbol{\varepsilon}-\boldsymbol{\varepsilon}^{vp})\\ &+(\boldsymbol{\varepsilon}-\boldsymbol{\varepsilon}^{vp}-\boldsymbol{\varepsilon}^i)^T\boldsymbol{\Gamma}\sum_M\left(\frac{\partial\mathbb{C}_e}{\partial d_M}\dot{d}_M\right)\boldsymbol{\Gamma}(\boldsymbol{\varepsilon}-\boldsymbol{\varepsilon}^{vp}-\boldsymbol{\varepsilon}^i)\Bigg). \end{aligned} \tag{A.15}$$

The derivative of $\mathbb{C}_e$ with respect to d_M can be rewritten as

$$\frac{\partial\mathbb{C}_e}{\partial d_M}=-\mathbb{C}_e\frac{\partial\mathbb{H}}{\partial d_M}\mathbb{C}_e, \tag{A.16}$$

therefore, Eq. (A.15) yields

$$\begin{aligned} -\sum_M\frac{\partial\Psi}{\partial d_M}\dot{d}_M=\frac{1}{2}\Bigg(&(\boldsymbol{\varepsilon}-\boldsymbol{\varepsilon}^{vp})^T\sum_M\left(\mathbb{C}_e\frac{\partial\mathbb{H}}{\partial d_M}\mathbb{C}_e\dot{d}_M\right)(\boldsymbol{\varepsilon}-\boldsymbol{\varepsilon}^{vp})\\ &+(\boldsymbol{\varepsilon}-\boldsymbol{\varepsilon}^{vp}-\boldsymbol{\varepsilon}^i)^T\boldsymbol{\Gamma}\sum_M\left(\mathbb{C}_e\frac{\partial\mathbb{H}}{\partial d_M}\mathbb{C}_e\dot{d}_M\right)\boldsymbol{\Gamma}(\boldsymbol{\varepsilon}-\boldsymbol{\varepsilon}^{vp}-\boldsymbol{\varepsilon}^i)\Bigg). \end{aligned} \tag{A.17}$$

$\mathbb{C}_e$ is a positive semi-definite matrix as proved in Appendix A.1. The non-negativity of $\partial_{d_M}(\mathbb{H})$ can be demonstrated by the non-negativity of their eigenvalues [81]. The eigenvalues of $\partial_{d_\ell}(\mathbb{H})$ are

$$\begin{aligned} &\lambda_{\partial_{d_\ell}(\mathbb{H})_1}=\frac{1}{E_{11}(1-d_\ell)^2}>0\\ &\lambda_{\partial_{d_\ell}(\mathbb{H})_{2-6}}=0, \end{aligned} \tag{A.18}$$

the eigenvalues of $\partial_{d_t}(\mathbb{H})$ are

$$\begin{aligned} &\lambda_{\partial_{d_t}(\mathbb{H})_1}=\frac{1}{E_t(1-d_t)^2}>0\\ &\lambda_{\partial_{d_t}(\mathbb{H})_{2-6}}=0, \end{aligned} \tag{A.19}$$

the eigenvalues of $\partial_{d_{st}}(\mathbb{H})$ are

$$\begin{aligned} &\lambda_{\partial_{d_{st}}(\mathbb{H})_1}=\frac{1}{G_t(1-d_{st})^2}>0\\ &\lambda_{\partial_{d_{st}}(\mathbb{H})_2}=\frac{1}{2}\lambda_{\partial_{d_{st}}(\mathbb{H})_1}>0\\ &\lambda_{\partial_{d_{st}}(\mathbb{H})_{3-6}}=0, \end{aligned} \tag{A.20}$$

and the eigenvalues of $\partial_{d_{s\ell}}(\mathbb{H})$ are

$$\lambda_{\partial_{d_{s\ell}}(\mathbb{H})_{1-2}} = \frac{1}{G_{12}(1-d_{s\ell})^2} > 0$$
$$\lambda_{\partial_{d_{s\ell}}(\mathbb{H})_{3-6}} = 0. \tag{A.21}$$

Therefore, $\partial_{d_M}(\mathbb{H})$ is a positive semi-definite matrix:

$$\frac{\partial \mathbb{H}}{\partial d_M} \geq 0. \tag{A.22}$$

The non-negativity of the first summand term in Eq. (A.17) can be demonstrate since the transpose matrix of a symmetric matrix is equal to the matrix itself,

$$\mathbb{C}_e \frac{\partial \mathbb{H}}{\partial d_M} \mathbb{C}_e = \left(\mathbb{C}_e \frac{\partial \mathbb{H}}{\partial d_M} \mathbb{C}_e \right)^T, \tag{A.23}$$

then,

$$\mathbb{C}_e \frac{\partial \mathbb{H}}{\partial d_M} \mathbb{C}_e \dot{d}_M \geq 0, \tag{A.24}$$

since $\dot{d}_M \geq 0$ because the damage is irreversible. Using the same procedure, the non-negativity of the second summand term in Eq. (A.17) yields

$$\boldsymbol{\Gamma} \mathbb{C}_e \frac{\partial \mathbb{H}}{\partial d_M} \mathbb{C}_e \boldsymbol{\Gamma} = \left(\boldsymbol{\Gamma} \mathbb{C}_e \frac{\partial \mathbb{H}}{\partial d_M} \mathbb{C}_e \boldsymbol{\Gamma} \right)^T, \tag{A.25}$$

and therefore,

$$\boldsymbol{\Gamma} \mathbb{C}_e \frac{\partial \mathbb{H}}{\partial d_M} \mathbb{C}_e \boldsymbol{\Gamma} \dot{d}_M \geq 0. \tag{A.26}$$

Finally, the mechanical energy dissipated by a viscodamage process is a product of a positive semi-definite matrices and an arbitrary vector [81]. For example, the left hand side terms in Eq. (A.23) is positive semi-definite matrix multiplied by $(\boldsymbol{\varepsilon} - \boldsymbol{\varepsilon}^{vp})$, then

$$(\boldsymbol{\varepsilon} - \boldsymbol{\varepsilon}^{vp})^T \sum_M \left(\mathbb{C}_e \frac{\partial \mathbb{H}}{\partial d_M} \mathbb{C}_e \dot{d}_M \right) (\boldsymbol{\varepsilon} - \boldsymbol{\varepsilon}^{vp}) \geq 0. \tag{A.27}$$

Similar, the left hand side terms in Eq. (A.25) is positive semi-definite matrix multiplied by $(\boldsymbol{\varepsilon} - \boldsymbol{\varepsilon}^{vp} - \boldsymbol{\varepsilon}^{i})$, hence

$$(\boldsymbol{\varepsilon} - \boldsymbol{\varepsilon}^{vp} - \boldsymbol{\varepsilon}^{i})^T \boldsymbol{\Gamma} \sum_M \left(\mathbb{C}_e \frac{\partial \mathbb{H}}{\partial d_M} \mathbb{C}_e \dot{d}_M \right) \boldsymbol{\Gamma} (\boldsymbol{\varepsilon} - \boldsymbol{\varepsilon}^{vp} - \boldsymbol{\varepsilon}^{i}) \geq 0. \tag{A.28}$$

Therefore, the mechanical energy dissipated due to a viscodamage process is equal to or greater than zero.

A.4. Thermodynamic restrictions of the material properties

The thermodynamic restrictions to ensure the non-negativity of the mechanical energy dissipated presented in Eq. (A.1) can be divided in three main groups: viscoelastic restrictions, viscoplastic restrictions and viscodamage restrictions. They are presented in the previous subsections of this appendix. Then, the restrictions are summarised, the one from the viscoelastic mechanical energy dissipated reads

$$\begin{aligned} \boldsymbol{\tau}^{ve} &\geq 0. \\ E_{11}, E_{22}, G_{12} &> 0 \\ |\nu_{23}| &< 1 \\ |\nu_{12}| &< \sqrt{\frac{E_{11}}{E_{22}}} \\ -1 < \nu_{23} &< 1 - 2\nu_{12}^2 \frac{E_{11}}{E_{22}}. \end{aligned} \tag{A.29}$$

The restrictions from the viscoplastic mechanical energy dissipated are

$$\begin{aligned} \hat{Y}_{CP}, \hat{Y}_{TP}, \hat{S}_{LP}, \hat{\mu}_{tp} &\geq 0 \\ 0 \leq \hat{\mu}_{s\ell p} &\leq 1 \\ \hat{Y}_{TP} &\leq \hat{Y}_{CP} \\ \frac{1 + \frac{\hat{\mu}_{tp}}{1+\hat{\mu}_{tp}}}{1 - \frac{\hat{\mu}_{tp}}{1+\hat{\mu}_{tp}}} &\leq \frac{\hat{Y}_{CP}}{\hat{Y}_{TP}}. \end{aligned} \tag{A.30}$$

Finally, the restrictions imposed from a viscodamage process are those defined in Eq. (A.29), except the first conditions, and

$$0 \leq d_M \leq 1. \tag{A.31}$$

References

[1] M.A. Karataş, H. Gökkaya, A review on machinability of carbon fiber reinforced polymer (CFRP) and glass fiber reinforced polymer (GFRP) composite materials, Def. Technol. 14 (2018) 318–326, http://dx.doi.org/10.1016/j.dt.2018.02.001.

[2] M.H. Hamidon, M.T. Sultan, A.H. Ariffin, A.U. Shah, Effects of fibre treatment on mechanical properties of kenaf fibre reinforced composites: A review, J. Mater. Res. Technol. 8 (2019) 3327–3337, http://dx.doi.org/10.1016/j.jmrt.2019.04.012.

[3] K. Friedrich, A.A. Almajid, Manufacturing aspects of advanced polymer composites for automotive applications, Appl. Compos. Mater. 20 (2013) 107–128, http://dx.doi.org/10.1007/s10443-012-9258-7.

[4] D.H. Kim, D.H. Choi, H.S. Kim, Design optimization of a carbon fiber reinforced composite automotive lower arm, Composites B 58 (2014) 400–407, http://dx.doi.org/10.1016/j.compositesb.2013.10.067.

[5] D.H. Kim, H.G. Kim, H.S. Kim, Design optimization and manufacture of hybrid glass/carbon fiber reinforced composite bumper beam for automobile vehicle, Compos. Struct. 131 (2015) 742–752, http://dx.doi.org/10.1016/j.compstruct.2015.06.028.

[6] C. Fragassa, A. Pavlovic, G. Minak, On the structural behaviour of a CFRP safety cage in a solar powered electric vehicle, Compos. Struct. 252 (2020) http://dx.doi.org/10.1016/j.compstruct.2020.112698.

[7] E. Amasawa, M. Hasegawa, N. Yokokawa, H. Sugiyama, M. Hirao, Environmental performance of an electric vehicle composed of 47% polymers and polymer composites, Sustain. Mater. Technol. 25 (2020) http://dx.doi.org/10.1016/j.susmat.2020.e00189.

[8] N. Fantuzzi, M. Bacciocchi, D. Benedetti, J. Agnelli, The use of sustainable composites for the manufacturing of electric cars, Compos. Part C: Open Access 4 (2021) http://dx.doi.org/10.1016/j.jcomc.2020.100096.

[9] A.K. Mohanty, S. Vivekanandhan, N. Tripathi, P. Roy, M.R. Snowdon, L.T. Drzal, M. Misra, Sustainable composites for lightweight and flame retardant parts for electric vehicles to boost climate benefits: A perspective, Compos. Part C: Open Access 12 (2023) http://dx.doi.org/10.1016/j.jcomc.2023.100380.

[10] S. Heimbs, Computational methods for bird strike simulations: A review, Comput. Struct. 89 (2011) 2093–2112, http://dx.doi.org/10.1016/j.compstruc.2011.08.007.

[11] J. Liu, Y. Li, X. Yu, X. Gao, Z. Liu, Design of aircraft structures against threat of bird strikes, Chin. J. Aeronaut. 31 (2018) 1535–1558, http://dx.doi.org/10.1016/j.cja.2018.05.004.

[12] D.H. Kim, S.Y. Kang, H.J. Kim, H.S. Kim, Strain rate dependent mechanical behavior of glass fiber reinforced polypropylene composites and its effect on the performance of automotive bumper beam structure, Composites B 166 (2019) 483–496, http://dx.doi.org/10.1016/j.compositesb.2019.02.053.

[13] Q. Liu, Y. Lu, J. Jiang, X. Yan, Q. Li, Experimental and numerical investigation into the dynamic impact responses of CFRP header rail, Thin-Walled Struct. 181 (2022) http://dx.doi.org/10.1016/j.tws.2022.110069.

[14] H.M. Hsiao, I.M. Daniel, R.D. Cordes, Strain rate effects on the transverse compressive and shear behavior of unidirectional composites, J. Compos. Mater. 33 (1999) 1620–1642, http://dx.doi.org/10.1177/002199839903301703.

[15] H. Koerber, J. Xavier, P.P. Camanho, High strain rate characterisation of unidirectional carbon-epoxy IM7-8552 in transverse compression and in-plane shear using digital image correlation, Mech. Mater. 42 (2010) 1004–1019, http://dx.doi.org/10.1016/j.mechmat.2010.09.003.

[16] H. Körber, Mechanical Response of Advanced Composites Under High Strain Rates (Ph.D. thesis), University of Porto, 2010.

[17] I.M. Daniel, J.M. Cho, B.T. Werner, J.S. Fenner, Characterization and constitutive modeling of composite materials under static and dynamic loading, AIAA J. 49 (2011) 1658–1664, http://dx.doi.org/10.2514/1.J050797.

[18] J.R. Vinson, E. Woldesenbet, Fiber orientation effects on high strain rate properties of graphite/epoxy composites, J. Compos. Mater. 35 (2001) 509–521, http://dx.doi.org/10.1106/21E5-2P22-GDWP-VC5C.

[19] H. Koerber, P. Kuhn, M. Ploeckl, F. Otero, P.W. Gerbaud, R. Rolfes, P.P. Camanho, Experimental characterization and constitutive modeling of the non-linear stress–strain behavior of unidirectional carbon–epoxy under high strain rate loading, Adv. Model. Simul. Eng. Sci. 5 (2018) http://dx.doi.org/10.1186/s40323-018-0111-x.

[20] H. Cui, D. Thomson, A. Pellegrino, J. Wiegand, N. Petrinic, Effect of strain rate and fibre rotation on the in-plane shear response of ±45° laminates in tension and compression tests, Compos. Sci. Technol. 135 (2016) 106–115, http://dx.doi.org/10.1016/j.compscitech.2016.09.016.

[21] F. Weng, Y. Fang, M. Ren, J. Sun, L. Feng, Effect of high strain rate on shear properties of carbon fiber reinforced composites, Compos. Sci. Technol. 203 (2021) http://dx.doi.org/10.1016/j.compscitech.2020.108599.

[22] M. Ploeckl, P. Kuhn, J. Grosser, M. Wolfahrt, H. Koerber, A dynamic test methodology for analyzing the strain-rate effect on the longitudinal compressive behavior of fiber-reinforced composites, Compos. Struct. 180 (2017) 429–438, http://dx.doi.org/10.1016/j.compstruct.2017.08.048.

[23] M.V. Hosur, J. Alexander, U.K. Vaidya, S. Jeelani, High strain rate compression response of carbon/epoxy laminate composites, Compos. Struct. 52 (2001) 405–417, http://dx.doi.org/10.1016/S0263-8223(01)00031-9.

[24] H. Koerber, P.P. Camanho, High strain rate characterisation of unidirectional carbon-epoxy IM7-8552 in longitudinal compression, Composites A 42 (2011) 462–470, http://dx.doi.org/10.1016/j.compositesa.2011.01.002.

[25] M. Ploeckl, P. Kuhn, H. Koerber, Characterization of unidirectional carbon fiber reinforced polyamide-6 thermoplastic composite under longitudinal compression loading at high strain rate, EPJ Web Conf. 94 (2015) http://dx.doi.org/10.1051/epjconf/20159401041.

[26] J.I. Perry, S.M. Walley, Measuring the effect of strain rate on deformation and damage in fibre-reinforced composites: A review, J. Dyn. Behav. Mater. 8 (2022) 178–213, http://dx.doi.org/10.1007/s40870-022-00331-0.

[27] J. Harding, L.M. Welsh, A tensile testing technique for fibre-reinforced composites at impact rates of strain, J. Mater. Sci. 18 (1983) 1810–1826, http://dx.doi.org/10.1007/BF00542078.

[28] N. Taniguchi, T. Nishiwaki, H. Kawada, Tensile strength of unidirectional CFRP laminate under high strain rate, Adv. Compos. Mater.: Off. J. Jpn. Soc. Compos. Mater. 16 (2007) 167–180, http://dx.doi.org/10.1163/156855107780918937.

[29] G.C. Jacob, J.M. Starbuck, J.F. Fellers, S. Simunovic, R.G. Boeman, Strain rate effects on the mechanical properties of polymer composite materials, J. Appl. Polym. Sci. 94 (2004) 296–301, http://dx.doi.org/10.1002/app.20901.

[30] L. Cheng, R. He, Y. Gao, H. Cui, Y. Li, Determination of fibre tension fracture toughness of composite laminates at high loading rate, Compos. Sci. Technol. 228 (2022) http://dx.doi.org/10.1016/j.compscitech.2022.109619.

[31] J. Hoffmann, H. Cui, N. Petrinic, Determination of the strain-energy release rate of a composite laminate under high-rate tensile deformation in fibre direction, Compos. Sci. Technol. 164 (2018) 110–119, http://dx.doi.org/10.1016/j.compscitech.2018.05.034.

[32] D.E. Sommer, D. Thomson, J. Hoffmann, N. Petrinic, Numerical modelling of quasi-static and dynamic compact tension tests for obtaining the translaminar fracture toughness of CFRP, Compos. Sci. Technol. 237 (2023) http://dx.doi.org/10.1016/j.compscitech.2023.109997.

[33] P. Kuhn, G. Catalanotti, J. Xavier, P.P. Camanho, H. Koerber, Fracture toughness and crack resistance curves for fiber compressive failure mode in polymer composites under high rate loading, Compos. Struct. 182 (2017) 164–175, http://dx.doi.org/10.1016/j.compstruct.2017.09.040.

[34] R.O. Ochola, K. Marcus, G.N. Nurick, T. Franz, Mechanical behaviour of glass and carbon fibre reinforced composites at varying strain rates, Compos. Struct. 63 (2004) 455–467, http://dx.doi.org/10.1016/S0263-8223(03)00194-6.

[35] K. Naresh, K. Shankar, B.S. Rao, R. Velmurugan, Effect of high strain rate on glass/carbon/hybrid fiber reinforced epoxy laminated composites, Composites B 100 (2016) 125–135, http://dx.doi.org/10.1016/j.compositesb.2016.06.007.

[36] P. Perzyna, The constitutive equations for rate sensitive plastic materials, Q. Appl. Math. 20 (1963) 321–332, http://dx.doi.org/10.1090/qam/144536.

[37] H. Kang, Y. Li, J. Liang, D. Thomson, H. Cui, Y. Li, Failure of short carbon-fiber-reinforced PEEK composites under high strain rate biaxial loading, Composites B 247 (2022) http://dx.doi.org/10.1016/j.compositesb.2022.110356.

[38] S. Eskandari, F.M.A. Pires, P.P. Camanho, H. Cui, N. Petrinic, A.T. Marques, Analyzing the failure and damage of FRP composite laminates under high strain rates considering visco-plasticity, Eng. Fail. Anal. 101 (2019) 257–273, http://dx.doi.org/10.1016/j.engfailanal.2019.03.008.

[39] W. Tan, B. Liu, A physically-based constitutive model for the shear-dominated response and strain rate effect of carbon fibre reinforced composites, Composites B 193 (2020) http://dx.doi.org/10.1016/j.compositesb.2020.108032.

[40] C. Shi, B. Guo, M. Sarıkaya, M. Çelik, P. Chen, M. Güden, Determination of the material model and damage parameters of a carbon fiber reinforced laminated epoxy composite for high strain rate planar compression, Int. J. Impact Eng. 149 (2021) http://dx.doi.org/10.1016/j.ijimpeng.2020.103771.

[41] W. Jin, Y. Zhang, L. Jiang, G. Yang, J. Chen, P. Li, A dynamic constitutive model and simulation of braided CFRP under high-speed tensile loading, Materials 15 (2022) http://dx.doi.org/10.3390/ma15186389.

[42] L. Raimondo, L. Iannucci, P. Robinson, P.T. Curtis, Modelling of strain rate effects on matrix dominated elastic and failure properties of unidirectional fibre-reinforced polymer-matrix composites, Compos. Sci. Technol. 72 (2012) 819–827, http://dx.doi.org/10.1016/j.compscitech.2012.02.011.

[43] I.M. Daniel, Constitutive behavior and failure criteria for composites under static and dynamic loading, Meccanica 50 (2015) 429–442, http://dx.doi.org/10.1007/s11012-013-9829-1.

[44] I.M. Daniel, Yield and failure criteria for composite materials under static and dynamic loading, Prog. Aerosp. Sci. 81 (2016) 18–25, http://dx.doi.org/10.1016/j.paerosci.2015.11.003.

[45] D. Ma, A. Manes, S.C. Amico, M. Giglio, Ballistic strain-rate-dependent material modelling of glass-fibre woven composite based on the prediction of a meso-heterogeneous approach, Compos. Struct. 216 (2019) 187–200, http://dx.doi.org/10.1016/j.compstruct.2019.02.102.

[46] B. Chang, X. Wang, Z. Long, Z. Li, J. Gu, S. Ruan, C. Shen, Constitutive modeling for the accurate characterization of the tension behavior of PEEK under small strain, Polym. Test. 69 (2018) 514–521, http://dx.doi.org/10.1016/j.polymertesting.2018.06.003.

[47] P.W. Gerbaud, F. Otero, P. Bussetta, P.P. Camanho, An invariant based transversely-isotropic constitutive model for unidirectional fibre reinforced composites considering the matrix viscous effects, Mech. Mater. 138 (2019) http://dx.doi.org/10.1016/j.mechmat.2019.103146.

[48] I.A.R. Lopes, P.P. Camanho, F.M.A. Pires, A. Arteiro, An invariant-based elasto-visco-plastic model for unidirectional polymer composites at finite strains, Int. J. Solids Struct. 236–237 (2022) http://dx.doi.org/10.1016/j.ijsolstr.2021.111292.

[49] M. Hegde, S.S. Mulay, An approach to model mechanical damage in particulate composites with viscoelastic matrix, Int. J. Adv. Eng. Sci. Appl. Math. 13 (2021) 79–88, http://dx.doi.org/10.1007/s12572-021-00289-7.

[50] I.R. Cózar, F. Otero, P. Maimí, E.V. González, S. Miot, A. Turon, P.P. Camanho, A three-dimensional plastic-damage model for polymer composite materials, Composites A 163 (2022) http://dx.doi.org/10.1016/j.compositesa.2022.107198.

[51] I.R. Cózar, F. Otero, P. Maimí, E.V. González, A. Turon, P.P. Camanho, An enhanced constitutive model to predict plastic deformation and multiple failure mechanisms in fibre-reinforced polymer composite materials, Compos. Struct. 330 (2024) http://dx.doi.org/10.1016/j.compstruct.2023.117696.

[52] A. Quintanas-Corominas, P. Maimí, E. Casoni, A. Turon, J.A. Mayugo, G. Guillamet, M. Vázquez, A 3D transversally isotropic constitutive model for advanced composites implemented in a high performance computing code, Eur. J. Mech. A Solids 71 (2018) 278–291, http://dx.doi.org/10.1016/j.euromechsol.2018.03.021.

[53] J.C. Simo, T.J.R.H. Springer, in: J. Marsden, L. Sirovich, S. Wiggins (Eds.), Computational Inelasticity, vol. 7, Springer, New York, NY, 1998, http://dx.doi.org/10.1007/b98904.

[54] S. Oller, Nonlinear Dynamics of Structures, Springer, 2014.

[55] C. Peyrac, T. Jollivet, N. Leray, F. Lefebvre, O. Westphal, L. Gornet, Self-heating method for fatigue limit determination on thermoplastic composites, 133, Elsevier Ltd, 2015, pp. 129–135, http://dx.doi.org/10.1016/j.proeng.2015.12.639,

[56] O.M. Heeres, A.S.J. Suiker, R.D. Borst, A comparison between the Perzyna viscoplastic model and the consistency viscoplastic model, Eur. J. Mech. A Solids 21 (2002) 1–12, http://dx.doi.org/10.1016/S0997-7538(01)01188-3.

[57] D. Perić, On a class of constitutive equations in viscoplasticity: Formulation and computational issues, Internat. J. Numer. Methods Engrg. 36 (1993) 1365–1393, http://dx.doi.org/10.1002/nme.1620360807.

[58] C. Miehe, J. Schröder, Comparative study of stress update algorithms for rate-independent and rate-dependent crystal plasticity, Internat. J. Numer. Methods Engrg. 50 (2001) 273–298, http://dx.doi.org/10.1002/1097-0207(20010120)50:2<273::AID-NME17>3.0.CO;2-Q.

[59] K. Nguyen, V.J. Amores, M.A. Sanz, F.J. Montáns, Thermodynamically consistent nonlinear viscoplastic formulation with exact solution for the linear case and well-conditioned recovery of the inviscid one, Comput. Mech. 67 (2021) 1349–1373, http://dx.doi.org/10.1007/s00466-021-01991-w.

[60] Y. Bai, T. Wierzbicki, Application of extended mohr-Coulomb criterion to ductile fracture, Int. J. Fract. 161 (2010) 1–20, http://dx.doi.org/10.1007/s10704-009-9422-8.

[61] D. Mohr, S.J. Marcadet, Micromechanically-motivated phenomenological Hosford-Coulomb model for predicting ductile fracture initiation at low stress triaxialities, Int. J. Solids Struct. 67–68 (2015) 40–55, http://dx.doi.org/10.1016/j.ijsolstr.2015.02.024.

[62] X. Kou, L. Li, X. Du, X. Zheng, Elastoplastic dynamic constitutive model of concrete with combined effects of temperature and strain rate, Case Stud. Construct. Mater. 18 (2023) http://dx.doi.org/10.1016/j.cscm.2023.e01905.

[63] P.P. Camanho, A. Arteiro, A.R. Melro, G. Catalanotti, M. Vogler, Three-dimensional invariant-based failure criteria for fibre-reinforced composites, Int. J. Solids Struct. 55 (2015) 92–107, http://dx.doi.org/10.1016/j.ijsolstr.2014.03.038.

[64] I.R. Cózar, J.M. Guerrero, P. Maimí, A. Arteiro, S. García-Rodríguez, M. Herman, A. Turon, Influence of unidirectional composite failure envelope shape on predicting compressive failure of a laminate with a filled-hole, Composites B 276 (2024) http://dx.doi.org/10.1016/j.compositesb.2024.111352.

[65] R. Panduranga, K. Shivakumar, Mode-II total fatigue life model for unidirectional IM7/8552 carbon/epoxy composite laminate, Int. J. Fatigue 94 (2017) 97–109, http://dx.doi.org/10.1016/j.ijfatigue.2016.09.014.

[66] ASTM, Standard Test Method for Density of Plastics by the Density-Gradient Technique. ASTM D1505, ASTM International, West Conshohocken, PA, 2018, http://dx.doi.org/10.1520/D1505-18.

[67] ASTM, Standard test methods for density and specific gravity (relative density) of plastics by displacement. ASTM D792, ASTM International, West Conshohocken, PA, 2020, http://dx.doi.org/10.1520/D0792-20.

[68] P.P. Camanho, P. Maimí, C.G. Dávila, Prediction of size effects in notched laminates using continuum damage mechanics, Compos. Sci. Technol. 67 (2007) 2715–2727, http://dx.doi.org/10.1016/j.compscitech.2007.02.005.

[69] ASTM, Standard test method for tensile properties of polymer matrix composite materials. ASTM D3039/D3039m, ASTM International, West Conshohocken, PA, 2017, http://dx.doi.org/10.1520/D3039_D3039M-17.

[70] ASTM, Standard Test Method for In-Plane Shear Response of Polymer Matrix Composite Materials by Tensile Test of a ±45° Laminate. ASTM D3518/D3518M-18, ASTM International, West Conshohocken, PA, 2018, http://dx.doi.org/10.1520/D3518_D3518M-18.

[71] I.R. Cózar, J.J. Arbeláez-Toro, P. Maimí, F. Otero, E.V. González, A. Turon, P.P. Camanho, A novel methodology to measure the transverse Poisson's ratio in the elastic and plastic regions for composite materials, Composites B 272 (2024) http://dx.doi.org/10.1016/j.compositesb.2023.111098.

[72] M. Vogler, R. Rolfes, P.P. Camanho, Modeling the inelastic deformation and fracture of polymer composites-part I: Plasticity model, Mech. Mater. 59 (2013) 50–64, http://dx.doi.org/10.1016/j.mechmat.2012.12.002.

[73] ASTM, Standard Test Method for Compressive Properties of Polymer Matrix Composite Materials Using a Combined Loading Compression (CLC) test fixture. ASTM D6641/D6641M, ASTM International, West Conshohocken, PA, 2018, http://dx.doi.org/10.1520/D6641_D6641M-16.

[74] G. Catalanotti, P.P. Camanho, A.T. Marques, Three-dimensional failure criteria for fiber-reinforced laminates, Compos. Struct. 95 (2013) 63–79, http://dx.doi.org/10.1016/j.compstruct.2012.07.016.

[75] A. Ortega, P. Maimí, E.V. González, J.R.S. de Aja, F.M. de la Escalera, P. Cruz, Translaminar fracture toughness of interply hybrid laminates under tensile and compressive loads, Compos. Sci. Technol. 143 (2017) 1–12, http://dx.doi.org/10.1016/j.compscitech.2017.02.029.

[76] R. Gutkin, S. Pinho, Practical application of failure models to predict the response of composite structures, in: ICCM International Conferences on Composite Materials, 2011.

[77] ASTM, Standard Test Method for Mode I Interlaminar Fracture Toughness of Unidirectional Fiber-Reinforced Polymer Matrix Composites. ASTM D5528/D5528M, ASTM International, West Conshohocken, PA, 2022, http://dx.doi.org/10.1520/D5528_D5528M-21.

[78] J. Wiegand, Constitutive Modelling of Composite Materials Under Impact Loading (Ph.D. thesis), University of Oxford, 2008.

[79] SIMULIA, ABAQUS User's Manual, Version 2022, Dassault Systèmes Simulia Corp, 2022, URL www.3ds.com.

[80] E.V. González, P. Maimí, E. Martín-Santos, A. Soto, P. Cruz, F.M. de la Escalera, J.R.S. de Aja, Simulating drop-weight impact and compression after impact tests on composite laminates using conventional shell finite elements, Int. J. Solids Struct. 144–145 (2018) 230–247, http://dx.doi.org/10.1016/j.ijsolstr.2018.05.005.

[81] G. Strang, Linear algebra and its applications fourth edition, Thomson, Brooks/Cole, 2006.

[82] J. Lemaitre, A continuous damage mechanics model for ductile fracture, J. Eng. Mater. Technol. 107 (1985) 83–89, http://dx.doi.org/10.1115/1.3225775.